

# Attributed-graphs kernel implementation using local detuning of neutral-atoms Rydberg Hamiltonian

Mehdi Djellabi,<sup>1</sup> Matthias Hecker,<sup>1</sup> and Shaheen Acheche<sup>1</sup>

<sup>1</sup>*Pasqal, 24 avenue Emile Baudot, 91120 Palaiseau*

(Dated: September 12, 2025)

We extend the quantum-feature kernel framework, which relies on measurements of graph-dependent observables, along three directions. First, leveraging neutral-atom quantum processing units (QPUs), we introduce a scheme that incorporates attributed graphs by embedding edge features into atomic positions and node features into local detuning fields of a Rydberg Hamiltonian. We demonstrate both theoretically and empirically that local detuning enhances kernel expressiveness. Second, in addition to the existing quantum evolution kernel (QEK), which uses global observables, we propose the generalized-distance quantum-correlation (GDQC) kernel, based on local observables. While the two kernels show comparable performance, we show that GDQC can achieve higher expressiveness. Third, instead of restricting to observables at single time steps, we combine information from multiple stages of the quantum evolution via pooling operations. Using extensive simulations on two molecular benchmark datasets, MUTAG and PTC\_FM, we find: (a) QEK and GDQC perform competitively with leading classical algorithms; and (b) pooling further improves performance, enabling quantum-feature kernels to surpass classical baselines. These results show that node-feature embedding and kernel designs based on local observables advance quantum-enhanced graph machine learning on neutral-atom devices.

## I. INTRODUCTION

Graph-structured data arise in domains as diverse as social media [1], chemistry [2], and program analysis [3], yet their intrinsic metric (shortest path distance) is discrete and non-Euclidean, rendering classical vector-space similarities inadequate. Furthermore, exact combinatorial measures such as graph isomorphism or graph-edit distance offer perfect discrimination, but even with state-of-the-art heuristic accelerations they become computationally prohibitive as graphs grow larger [4]. To obtain tractable and differentiable notions of similarity, the field has turned to graph kernels, which embed graphs into a reproducing-kernel Hilbert space where powerful kernel methods apply. The seminal survey of [5] unified random-walk and other early kernels, while the Weisfeiler-Leman family leveraged color refinement to scale sub-tree comparisons to large graphs [6]. Complementary work casts graph comparison as an optimal-transport problem aligning intra-graph metric structures and gracefully handles graphs of differing sizes, proving effective for biological and social networks [7]. More precisely, these developments fit within the broader program of geometric deep learning, which generalizes representation-learning techniques to non-Euclidean domains [8].

More recently, interest has surged in mapping graphs to quantum systems and computing similarities directly from physical measurements. Early work framed the evolution of a continuous-time quantum walk as a positive-definite kernel on graphs [9, 10], and subsequent extensions employed discrete-time walks and information-theoretic divergences to enrich the feature space [11]. Modern quantum platforms now encode each graph as a parameterized quantum state and estimate kernel entries via repeated state-overlap measurements, a strategy validated experimentally on a 10-qubit nuclear-magnetic-resonance processor [12]. Complementing these hardware demonstrations, industry toolkits such as Pasqal’s open-source Quantum Evolution Kernel (QEK) [13, 14] make

quantum-enhanced graph machine-learning pipelines accessible on neutral-atom devices [15]. Together, these developments suggest that quantum hardware may soon deliver graph kernels with higher expressive power and lower sample complexity than their classical counterparts, reinforcing the motivation for the methods introduced here. Despite this notable progress the graph-kernel literature from the perspective of quantum computing remains strongly skewed towards unattributed graphs. Kernels that focus on attributed graphs with discrete labels attached to vertices and edges have been studied comparatively few [16].

Quantum feature kernels such as used in the QEK algorithm represent a particular class of quantum kernels within which the quantum features are derived from measured observables. Herein, a graph  $\mathcal{G}$  is embedded into the system Hamiltonian  $\hat{H}^{\mathcal{G}}$  such that a time evolution imposes the graph information onto the quantum state  $|\psi_{\mathcal{G}}(t)\rangle$ , and eventually onto any measured observable  $O_{\alpha}^{\mathcal{G}}(t) = \langle \psi_{\mathcal{G}}(t) | \hat{O}_{\alpha} | \psi_{\mathcal{G}}(t) \rangle$ . For the purpose of a quantum feature kernel, multiple observables can be considered ( $\alpha = 1, \dots, N_M$ ) and measurements can be taken at multiple time steps ( $t_1, \dots, t_{N_t}$ ). In combination, they provide the  $(N_M N_t)$ -dimensional quantum-feature vector  $\mathbf{O}^{\mathcal{G}}$  which encodes the graph information in a non-trivial way. This allows to generically define a quantum feature kernel between two graphs of a given dataset,  $\mathcal{G}_{\mu}$  and  $\mathcal{G}_{\mu'}$ , as

$$K_{\mu\mu'} = \kappa(\mathcal{G}_{\mu}, \mathcal{G}_{\mu'}) = F_{\kappa}[\mathbf{O}^{\mathcal{G}_{\mu}}, \mathbf{O}^{\mathcal{G}_{\mu'}}]. \quad (1)$$

The kernel function  $F_{\kappa}$  can be chosen in many ways. It only needs to ensure kernel properties like positive semi-definiteness (PSD), *i.e.* all eigenvalues of  $K$  have to be non-negative.

In this work, we expand on the attributed-graphs toolset by introducing an implementation scheme that allows quantum feature kernels (1) to deal with node attributes. Specifically, we use the local detuning of a neutral-atom Rydberg Hamiltonian to encode node features. We demonstrate that corresponding features kernels (1) are more expressive than

without encoded node features, and we present extensive numerical comparison between both scenarios on two well-known benchmark datasets, MUTAG and PTC\_FM. Furthermore, this work includes a study of different kernel functions  $F_\kappa$ , whereby two conceptually different implementations are tested, namely QEK and the Generalized-Distance Quantum-Correlation (GDQC) kernel. In contrast to the established QEK kernel which exploits a global observable, the proposed GDQC kernel draws from a local observable, the correlation matrix and is inspired by the classical generalized-distance Weisfeiler-and-Leman (GD-WL) kernel [6]. Lastly, we add one more layer of enhanced expressive power to the project: pooling. Specifically, we combine kernels computed by observables measured at multiple time steps by means of pooling operations. Hereby, two different pooling schemes are tested, sum pooling and product pooling. Having trained a support vector machine (SVM) using all these different kernel implementations, the results of the extensive numerical tests are presented in section IV, and discussed. We observe a trend that the kernels using node features generally yield better SVM predictions compared to the node-agnostic ones. Among the quantum-feature kernels, QEK and GDQC, we observe comparative performances which are competitive with the classical baselines. However, we find that pooling can enhance their performance and enable them to outperform the classical algorithms.

This paper is organized as follows: In Sec. II we detail all aspects of the graph-feature extraction. We introduce the neutral-atom Rydberg Hamiltonian (II A), introduce the attributed-graphs embedding scheme (II B), and present all details concerning the emulation (II C). In Sec. III we discuss classical kernel methods used for the baselines before we introduce the quantum kernel functions  $F_\kappa$  used in this work. We revisit the QEK kernel (III A), introduce the proposed GDQC kernel (III B), before we define the two pooling schemes in part III C. In Sec. IV, the numerical results are presented and discussed. Finally, we provide a conclusion in Sec. V. In App. A we rigorously demonstrate that the kernels with node-feature embedding are more expressive than the ones without. Apps. B and C prove, respectively, that the GDQC kernel satisfies all kernel properties and that it is as expressive as the GD-WL kernel. In App. D we prove that the inclusion of different time steps can only increase the kernel expressiveness.

## II. QUANTUM FEATURE EXTRACTION

In this section we demonstrate how the quantum features  $\mathcal{O}^G$  [cf. Eq. (1)] are extracted using a neutral-atom QPU. After introducing the Rydberg Hamiltonian, we discuss the graph embedding scheme, and explain the details of the emulation used to extract the graph-dependent observables.

### A. Rydberg/ Ising Hamiltonian

Neutral-atom quantum computing processors (QPU) are operated such that the two states describing a qubit, the zero state

$|0\rangle$  and the one-state  $|1\rangle$ , correspond to particularly chosen long-lived atomic energy levels where specifically the state  $|1\rangle$  is associated with a highly-excited atomic Rydberg level. For example, for  $^{87}\text{Rb}$  atoms, commonly used in the field, one such choice is given through  $|0\rangle = |5S_{1/2}, F=2, m_F=2\rangle$  and  $|1\rangle = |6S_{1/2}, m_J=1/2\rangle$ . This choice leads to an effective Ising Hamiltonian where the long-ranged interaction is driven through the van-der-Waals interaction of distant atoms which are simultaneously in the highly-excited and spatially extended Rydberg state. As a consequence, a system of  $N$  atoms is described through the so-called Rydberg Hamiltonian [17]

$$\hat{\mathcal{H}}(\mathbb{J}, \Omega, \delta) = \frac{1}{2} \sum'_{i,j} J_{ij} \hat{n}_i \hat{n}_j + \hbar \sum_{i=1}^N \left( \frac{\Omega}{2} \hat{\sigma}_i^x - \delta_i \hat{n}_i \right), \quad (2)$$

where the summation  $\sum'_{i,j} = \sum_{i,j=1}^N |j \neq i|$  is restricted to non-identical indices. The coupling constant  $J_{ij} = C_6/r_{ij}^6$  describes the strength of the van-der-Waals interaction between atoms  $i$  and  $j$  which are separated by a distance  $r_{ij}$ , and  $\mathbb{J}$  denotes the respective  $N \times N$ -dimensional matrix with  $\mathbb{J}_{ij} = J_{ij}$ . The positive constant  $C_6$  depends on the Rydberg level, and in the chosen configuration its value is  $C_6/\hbar = 865723 \text{ rad } \mu\text{s}^{-1} \mu\text{m}^6$  (corresponding to the Rydberg level  $n=60$ ). The external fields, the Rabi frequency  $\Omega$  and the spatially-dependent detuning  $\delta = (\delta_1, \dots, \delta_N)$ , are primarily determined by the laser frequencies and intensities which drive the atomic system. Throughout this work, we set the Rabi frequency to  $\Omega = 2\pi \text{ rad } / \mu\text{s}$ . The Hilbert space which the Hamiltonian (2) acts on is  $2^N$  dimensional. Using the occupational (or measurement) basis, a basis vector is given through  $|\mathbf{b}\rangle = |b_1 b_2 \dots b_N\rangle$  where each entry takes on values  $b_i \in \{0, 1\}$ . The action of the Pauli-matrix operators in (2) on a basis state is given by  $\hat{n}_i |b_i\rangle = b_i |b_i\rangle$ ,  $\hat{\sigma}_i^x |b_i\rangle = |1-b_i\rangle$  and  $\hat{\sigma}_i^z |b_i\rangle = (-1)^{b_i} |b_i\rangle$  given that also  $\hat{n}_i = (1 - \hat{\sigma}_i^z)/2$ . The last relation can be used to translate the Hamiltonian (2) into the standard Ising representation

$$\hat{\mathcal{H}}(\mathbb{J}, \Omega, \delta) = \frac{1}{8} \sum'_{i,j} J_{ij} \hat{\sigma}_i^z \hat{\sigma}_j^z + \hbar \sum_{i=1}^N \left( \frac{\Omega}{2} \hat{\sigma}_i^x + h_i^z \hat{\sigma}_i^z \right) + \bar{E}, \quad (3)$$

where the constant  $\bar{E} = \text{tr}\{\hat{\mathcal{H}}\}/2^N = \frac{1}{8} \sum'_{i,j} J_{ij} - \frac{1}{2} \hbar \sum_i \delta_i$  denotes the average energy, and the longitudinal field is given by

$$h_i^z = \frac{1}{2} \delta_i - \frac{1}{4\hbar} \sum_{j \neq i} J_{ij}. \quad (4)$$

The Ising Hamiltonian (3) with its more symmetric representation can be more revealing for a physical intuition, as we will demonstrate in part II B.

By design, the initial state in a neutral-atom QPU is the all-zero state  $|\psi(0)\rangle = |0\rangle$ . With the Hamiltonian (2) being time independent, the time evolution corresponds to a quench experiment, whereby the time-evolved state is given by

$$|\psi(t)\rangle = \exp \left[ -i(t/\hbar) \hat{\mathcal{H}}(\mathbb{J}, \Omega, \delta) \right] |\psi(0)\rangle. \quad (5)$$

The interest of the current work lies in three specific observables which will serve as the quantum features  $\mathcal{O}^{\mathcal{G}}$  [cf. Eq. (1)]: the excitation number  $n_i(t)$ , the correlation matrix  $C_{ij}(t)$ , and the probability for a fixed number  $k$  of excitations  $P_k(t)$ . These observables are defined as

$$\begin{aligned} P_k(t) &= \langle \psi(t) | \hat{P}_k | \psi(t) \rangle, \quad n_i(t) = \langle \psi(t) | \hat{n}_i | \psi(t) \rangle, \\ C_{ij}(t) &= \langle \psi(t) | \hat{n}_i \hat{n}_j | \psi(t) \rangle, \end{aligned} \quad (6)$$

where the projection operator onto a fixed-excitation subspace is defined as  $\hat{P}_k = \sum_{\mathbf{b}} \delta_{k, \sum_i b_i} |\mathbf{b}\rangle \langle \mathbf{b}|$  with the Kronecker delta  $\delta_{k, k'}$  and  $k = 0, 1, \dots, N$ . All observables (6) are diagonal in the measurement basis, and thus, they can be easily sampled after each run of the neutral-atom QPU.

## B. Attributed-graphs embedding

In the present work we deal with graphs that originate from two common benchmark datasets for binary classification: mutagenic aromatic and heteroaromatic nitro compounds (MUTAG) consisting of a total of 188 molecules with the task of predicting whether a molecule is mutagenic on *Salmonella typhimurium* or not, and predictive toxicology challenge – female mice (PTC\_FM) consisting of 349 molecules with the task of predicting if a compound is carcinogenic [18–20]. In both datasets the compounds are provided as attributed graphs  $\mathcal{G} = (\mathcal{V}, \mathcal{E}, \mathcal{L})$ , also referred to as labeled graphs or heterogeneous graphs, with a set of nodes  $\mathcal{V}$  (the atoms), a set of edges  $\mathcal{E}$  (the bonds between atoms), and a set of node labels  $\mathcal{L}$  (the name of the atoms) where the latter are interchangeably referred to as labels, attributes or features.

A common strategy to embed a graph onto the Hamiltonian (2) is by choosing the atom’s positions such that connected atoms have a significant coupling strength  $J_{ij}$  whereas unconnected atoms are coupled with a negligible strength. Mathematically, we introduce the graph-dependent coupling matrix as

$$\mathbb{J}_{ij}^{\mathcal{G}} = \begin{cases} J_{\text{NN}} & , (i, j) \in \mathcal{E} \\ J_{ij} \ll J_{\text{NN}} & , (i, j) \notin \mathcal{E} \end{cases} \quad (7)$$

where we defined the nearest-neighbor coupling strength  $J_{\text{NN}} = C_6/r_{\text{NN}}^6$  with  $r_{\text{NN}}$  being the nearest-neighbor distance. Throughout this study, we fix the nearest-neighbor distance to  $r_{\text{NN}} = 5 \mu\text{m}$  such that the nearest-neighbor coupling becomes  $J_{\text{NN}}/\hbar \approx 55.4 \text{ MHz}$ . The choice (7) is very appealing for the graph embedding. Yet, due to the Rydberg blockade mechanism [21, 22] only a certain class of graphs can be embedded via this scheme. These are the so-called unit-disk graphs wherein an edge between two nodes only exists if the distance between them is smaller than a fixed value [23]. In general, the task of finding a unit-disk graph embedding is a NP-complete problem [24]. Conveniently, the molecules in the dataset just like the atoms in the QPU interact through physical forces which naturally makes them unit-ball graphs. The only problem is the dimension. Current neutral-atom QPU only allow for two-dimensional registers. Therefore, in our study we only

include molecules that admit a two-dimensional embedding reducing the size of the datasets to 171 (MUTAG\*) and 312 (PTC\_FM\*) molecules. We denote the reduced datasets with an asterisk \*. The algorithm used to compute the layouts is an extension of the one described in Ref. [14] (appendix E therein).

The graph-dependent coupling matrix  $\mathbb{J}_{ij}^{\mathcal{G}}$  (7) only embeds the edges  $\mathcal{E}$  of the graph, but it makes no use of the node features  $\mathcal{L}$ . The embedding of the node features  $\mathcal{L}$  is a key element of this work. It is achieved through an appropriate choice of the local detuning  $\delta_i \rightarrow \delta_i^{\mathcal{G}}$ , see Eq. (2). Specifically, we have chosen a scheme that exploits the atomic masses  $m_i$  within the molecules, and we define

$$\delta_i^{\mathcal{G}} = \delta_0 m_C / m_i \leq \delta_0, \quad (8)$$

where  $\delta_0$  is a fixed offset value and  $m_C = 12 \text{ u}$  is the mass of a carbon atom, the lightest atom in the datasets (Note that hydrogen atoms are omitted in the graphs.). The atomic masses are obtained from PubChem Periodic Table webpage [25]. This allows us to study the graph-embedded Hamiltonian (2), once with the inclusion of the node-feature embedding (8), and once without. We define the respective Hamiltonians as the (global) Hamiltonian

$$\hat{\mathcal{H}}_{\text{glob}}^{\mathcal{G}} = \hat{\mathcal{H}}(\mathbb{J}^{\mathcal{G}}, \Omega, \delta_{\text{glob}}), \quad (9)$$

which is subjected to a globally fixed detuning value  $\delta_{\text{glob}} = (\delta_0, \dots, \delta_0)$ , and as the (local) Hamiltonian

$$\hat{\mathcal{H}}_{\text{loc}}^{\mathcal{G}} = \hat{\mathcal{H}}(\mathbb{J}^{\mathcal{G}}, \Omega, \delta^{\mathcal{G}}), \quad (10)$$

whose detuning  $\delta^{\mathcal{G}} = (\delta_1^{\mathcal{G}}, \dots, \delta_N^{\mathcal{G}})$  embeds the node features via Eq. (8). It is clear that a time evolution governed by a graph-dependent Hamiltonian, Eq. (9) or (10), leave an imprint of the graph on the time-evolved state via Eq. (5), and as a consequence, the measured observables (6) equally acquire a graph dependence. This explains how the measured observables encode a graph embedding, and why they can be meaningfully used in a graph kernel application, cf. Eq. (1).

The value of the fixed detuning  $\delta_0$  needs to be chosen appropriately such that the impact of the local-detuning embedding used in Eq. (10) is measurable. To estimate the magnitude we exploit the Ising representation of the Hamiltonian (3) wherein the longitudinal field value  $h_i^z$  (4) directly demonstrates that the local detuning field has to compete with a relatively strong local offset value. For the given molecules, one can approximate the offset value as  $\sum_{j \neq i} J_{ij}^{\mathcal{G}} \approx N_i^{\text{deg}} J_{\text{NN}}$  with  $N_i^{\text{deg}}$  being the degree of node  $i$  and for molecules  $N_i^{\text{deg}} \in \{1, 2, 3, 4\}$ . Hence, the longitudinal field becomes

$$h_i^z \approx \frac{1}{4\hbar} J_{\text{NN}} \left( -N_i^{\text{deg}} + \frac{2\hbar\delta_0}{J_{\text{NN}}} \frac{m_C}{m_i} \right). \quad (11)$$

Here, we note two things. First, in order for the local-detuning to be noticeable, one has to choose the offset value such that  $2\hbar\delta_0/J_{\text{NN}} = \mathcal{O}(1)$ . Second, we see that the offset value conveniently encodes the degree of each node as a default piece of information. We would not want to overshadow this

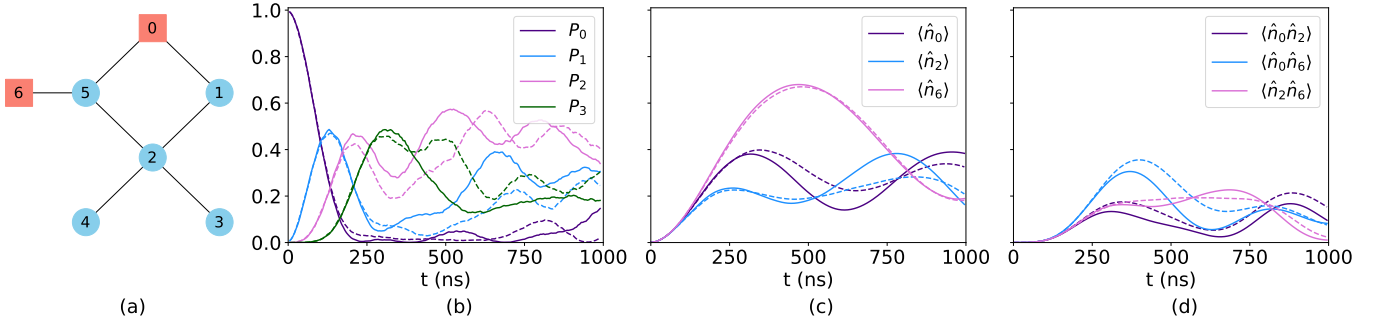


FIG. 1. Emulation results for the molecule in (a) consisting of five carbon (blue) and two oxygen (red) atoms. (b)-(d) Time evolution of the three observables introduced in Eq. (6), the excitation probability  $P_k$ , the excitation number  $n_i = \langle \hat{n}_i \rangle$  and the pairwise correlations  $C_{ij} = \langle \hat{n}_i \hat{n}_j \rangle$ . The solid (dashed) lines correspond to evolution subjected to the global-detuning (local-detuning) Hamiltonian, see Eq. (9) (Eq. (10)). For the given molecule and parameter values one observes differences between the two detuning cases starting at the latest after  $t \gtrsim 250$  ns. These differences can be learned by the machine learning models designed in trained in Secs. III and IV. The molecule in (a) belongs to the PTC\_FM\* dataset, and it has the SMILES representation "CC1(C)COC1=O".

embedded node information, but instead add a little value on top according to the node feature, *i.e.* according to the mass of atom  $i$ . For this reason, we consider an appropriate choice for the fixed detuning value as  $2\hbar\delta_0/J_{\text{NN}} \lesssim 0.3$ . The value we choose in this work is  $\delta_0 = \pi \text{ rad}/\mu\text{s}$ , such that  $2\hbar\delta_0/J_{\text{NN}} \approx 0.1$ .

### C. Emulation

With all the specifications provided we run two emulations for every graph in the reduced datasets MUTAG\* and PTC\_FM\*: Once where the time evolution is governed by the local-detuning Hamiltonian (10) and once governed by the global-detuning counterpart (9). At multiple time steps, we sample the three observables defined in Eq. (6), the probability for a fixed number of excitations  $P_k$ , the excitation number  $n_i$  and the correlation  $C_{ij}$ , with a number of shots  $N_{\text{shots}} = 1000$ . Their values form the set of feature vectors  $\mathcal{O}^{\mathcal{G}_\mu}$ , see Eq. (1), which are used in the machine learning tasks in Secs. IV and III. The emulation is computed using two open-source libraries: Pulser [26] and EMU-MPS [27]. Pulser is a Python toolkit for neutral-atom quantum computing that allows to program experiments directly at the pulse level. The package EMU-MPS provides an efficient, state-of-the-art emulation backend that emulates pulse-level dynamics of neutral-atom arrays by storing the state as a matrix product state.

In Fig. 1 we demonstrate the time evolution by presenting emulation results for a given molecule [panel (a)] of the PTC\_FM\* dataset. The three panels (a)-(c) show respectively, the excitation probability  $P_k$ , the excitation number  $n_i$  and the correlation matrix elements  $C_{ij} = \langle \hat{n}_i \hat{n}_j \rangle$ . To highlight the effect of the local detuning we compare the local-detuning results (dashed lines) with the global-detuning ones (solid lines). In all three observables one observes differences between the two cases emerging at the latest after  $t \gtrsim 250$  ns. Note that the presented molecule consists of five carbon and two oxygen molecules. The given implementation scheme is such that the

global-detuning Hamiltonian (9) effectively assumes that all atoms are carbon atoms ( $m_C = 12$  u). Thus, the oxygen nodes (0 and 6) are particularly interesting. Among the two excitation numbers  $n_0$  and  $n_6$ , only the node  $n_0$  with node degree two shows a significant deviation. During the research phase we have also tested a larger detuning value of  $\delta_0 = 2\pi \text{ rad}/\mu\text{s}$  which also enforces a strong deviation for  $n_6$ . Across the entire datasets however, this has only a minor effect as the prediction tasks in Sec. IV yield similar results. Note also that atoms heavier than oxygen ( $m_O = 16$  u) are significantly stronger influenced by the local detuning.

## III. GRAPH KERNEL METHODS FOR MACHINE LEARNING

In this section we introduce all the kernels used in this work: first, the classical kernels used for benchmarking; then, the quantum feature kernels, QEK (III A) and GDQC (III B). Lastly, in Subsec. III C we introduce the pooling operations that are employed.

Kernel-based machine learning methods rely on a rigorous mathematical framework grounded in the theory of Reproducing Kernel Hilbert Spaces (RKHS). The foundation is laid by the Moore-Aronszajn Theorem, which guarantees that every positive definite kernel defines a unique RKHS where the kernel acts as the reproducing kernel [28]. Within this space, the Representer Theorem shows that the solution to many regularized risk minimization problems can be written as a finite linear combination of kernel functions evaluated at the training points, thus reducing infinite-dimensional optimization to a tractable finite-dimensional one [29]. Furthermore, Mercer's Theorem [30] offers a spectral decomposition of continuous, symmetric, positive-definite kernels, interpreting them as inner products in high-dimensional feature spaces [31]. These results together enable the development of powerful nonlinear algorithms, such as Support Vector Machines (SVMs) [32], with solid theoretical guarantees and practical scalability, for various machine learning tasks such as classification and re-



gression. In practical terms these kernel methods allow SVMs to classify non-linearly separable data by implicitly mapping input features into a higher-dimensional space where a linear separator can be found, without the need of an explicit computation of the mapping [31].

Graph-based data are known to be a particular kind of data due to the non-Euclidean nature of their associated distance measure. This limits the scope of the types of kernels that can be used on graphs by putting additional constraint on their properties (see Sec. III B for more details). Therefore, researchers came up with graph-tailored kernels that are typically designed to overcome these limitations by capturing structural similarities. This is achieved, for example, by means of walks, subtrees, or subgraph patterns. By embedding graphs into Hilbert spaces while preserving their combinatorial properties, they provide a principled and flexible approach to graph machine learning tasks. From the vast literature of classical graph kernels, we employ the following ones for the benchmarking purposes:

*Random walk kernels.* These measure similarity between graphs by counting matching random walks in each graph, capturing detailed structural patterns. Introduced in Ref. [33], they offer expressiveness but can be computationally intensive and prone to tottering effects.

*k-core kernels.* These kernels measure similarity between graphs by comparing the distributions of their  $k$ -cores, which are defined as the maximal number of subgraphs where every node has a degree at least equal to  $k$ . The approach was proposed in Ref. [34] as part of structured representations for graphs.

*Shortest path kernel.* Introduced in Ref. [35] this kernel is an efficient alternative to random walks, capturing both local and global structures by evaluating pairs of nodes with matching shortest path lengths.

*Weisfeiler-Leman kernels.* Based on the Weisfeiler and Leman (WL) graph isomorphism test, these kernels iteratively update node labels based on neighborhood structures [6].

### A. Quantum evolution kernel (QEK)

First introduced by Henry *et al.* [13], the quantum evolution kernel (QEK) algorithm is a quantum-feature kernel implementation [see Eq. (1)] that draws from probability distributions generated from measured observables. Specifically, within the proof-of-principle implementation of Ref. [14], the algorithm draws from the global observable vector  $\mathbf{P}^{\mathcal{G}} = (P_0^{\mathcal{G}}(t), P_1^{\mathcal{G}}(t), P_2^{\mathcal{G}}(t), \dots)^{\top}$  with  $P_k^{\mathcal{G}}(t)$  being the excitation probability for a fixed number  $k$  of excitations at a given time  $t$ , see Eq. (6). The superscript  $\mathcal{G}$  indicates that the time evolution is subjected to a graph-embedded Hamiltonian, cf. Sec. II. To discriminate between two graphs,  $\mathcal{G}_{\mu}$  and  $\mathcal{G}_{\mu'}$ , the QEK algorithm implements the following kernel function

$$\kappa_{\text{QEK}}(\mathcal{G}_{\mu}, \mathcal{G}_{\mu'}) = \exp \left[ -\mu_0 \text{JS}(\mathbf{P}^{\mathcal{G}_{\mu}}, \mathbf{P}^{\mathcal{G}_{\mu'}}) \right]. \quad (12)$$

Here, the Jensen–Shannon divergence  $\text{JS}(\mathbf{P}, \mathbf{P}')$  measures the similarity between the two distributions. By construc-

tion, the kernel function (12) ensures positive definiteness. Throughout this work we fix the model parameter  $\mu_0 = 2$ .

Within its proof-of-principle implementation [14], the QEK kernel (12) has been applied to non-attributed graphs. Correspondingly, the time evolution has been subjected to a global-detuning Hamiltonian  $\hat{\mathcal{H}}_{\text{glob}}^{\mathcal{G}}$  (9). When coupled with a support vector machine (SVM), the QEK algorithm has matched the performance of leading state-of-the-art classical graph kernels on several benchmark datasets of small graphs [14]. Thereby, QEK’s capabilities have been demonstrated both, numerically via emulations as well as on real quantum hardware, on a 32-qubit neutral-atom processor.

In our work, we expand on the previous QEK implementation [14] twofold. First, and most importantly, we want it to be able to deal with attributed graphs. This is accomplished by changing the Hamiltonian that governs the time evolution from  $\hat{\mathcal{H}}_{\text{glob}}^{\mathcal{G}}$  (9) to the local-detuning Hamiltonian  $\hat{\mathcal{H}}_{\text{loc}}^{\mathcal{G}}$  (10). As described in Subsec. II B, the latter Hamiltonian embeds the atomic masses (the node features) into the local detuning  $\delta_i$ . As a result, we obtain an observable vector  $\mathbf{P}^{\mathcal{G}}$  which contains graph information drawn from both, the edges and the node features. Similar to before, the observable vectors are inserted into the kernel function (12). To distinguish the two cases, evolution under  $\hat{\mathcal{H}}_{\text{glob}}^{\mathcal{G}}$  and  $\hat{\mathcal{H}}_{\text{loc}}^{\mathcal{G}}$ , we use the notation  $\kappa_{\text{QEK}}^{\text{glob}}$  and  $\kappa_{\text{QEK}}^{\text{loc}}$ , respectively. Mathematically, switching from  $\kappa_{\text{QEK}}^{\text{glob}}$  to  $\kappa_{\text{QEK}}^{\text{loc}}$  has profound consequences which can be summarized by proposition 1 which is proven in App. A.

**Proposition 1.** *The quantum evolution kernel  $\kappa_{\text{QEK}}^{\text{loc}}$  is genuinely more expressive than  $\kappa_{\text{QEK}}^{\text{glob}}$  for distinguishing attributed graphs.*

The second extension to the QEK algorithm that we undertake lies in pooling of different time steps. The above implementation draws the excitation probability from a single time step  $t$ . In Subsec. III C we explain how multiple time steps can be united in order to combine information sampled from different regimes of the time evolution.

The excitation probability  $P_k^{\mathcal{G}}(t)$  (6) used in the QEK algorithm is a natural observable candidate to capture graph information as it is permutation invariant. Moreover, it is a global observable rendering it a useful tool to study global graph properties. However, if it comes to local graph properties the excitation probability  $P_k^{\mathcal{G}}(t)$  may not be the most convenient choice. An attempt to generalize the algorithm from the global observables  $P_k^{\mathcal{G}}(t)$  to observables that capture distributions of local subcomponents of a graph (*e.g.*, nodes or edges)—while maintaining permutation invariance—requires the fixing of a canonical ordering for each graph, a costly task known as the graph canonization problem [36]. This potential shortcoming of the QEK algorithm (12) has motivated the design of the generalized-distance quantum-correlation (GDQC) kernel, see Subsec. III B.

---

**Algorithm 1:** Computation of the GDQC feature vector  $\chi[C^\mathcal{G}(t), D^\mathcal{G}]$  in Eq. (13).

---

**Input:**  $C^\mathcal{G}(t); D^\mathcal{G}; N_{\text{bins}}^D; N_{\text{bins}}^C; \Delta_C = 1/N_{\text{bins}}^C;$   
 $\Delta_D = d_{\text{max}}/N_{\text{bins}}^D$   
**for**  $\ell \leftarrow 0$  **to**  $N_{\text{bins}}^D - 1$  **do**  
     $\Omega_\ell^{(d)} \leftarrow [\ell \Delta_D, (\ell + 1) \Delta_D]$   
    **for**  $p \leftarrow 0$  **to**  $N_{\text{bins}}^C - 1$  **do**  
         $\Omega_p^{(q)} \leftarrow [p \Delta_C, (p + 1) \Delta_C]$   
         $\chi[N_{\text{bins}}^C \ell + p] \leftarrow |\{(i, j) : D_{i,j}^\mathcal{G} \in \Omega_\ell^{(d)}, C_{i,j}^\mathcal{G}(t) \in \Omega_p^{(q)}\}|$   
**return**  $\chi / \|\chi\|$

---

**B. Generalized-distance quantum-correlation (GDQC) kernel**

In this part we introduce the new quantum-feature kernel which is used in this work, the generalized-distance quantum-correlation (GDQC) kernel. In contrast to the QEK algorithm which designed to excel at capturing global graph information, the new kernel draws from local observables making it more apt at predicting local graph properties.

The GDQC kernel is inspired by the classical generalized-distance Weisfeiler-and-Leman (GD-WL) kernel [6]. As such the goal is to combine the graph distance, *i.e.* distance  $d_G(i, j)$  between nodes  $i$  and  $j$  and  $D^\mathcal{G}$  being the distance matrix where  $D_{i,j}^\mathcal{G} = d_G(i, j)$ , with another piece of graph information. Within the GDQC framework, the second piece of information is a local observable. In the present work we use the correlation matrix  $C^\mathcal{G}(t)$  where  $C_{i,j}^\mathcal{G}(t) = \langle \psi_G(t) | \hat{n}_i \hat{n}_j | \psi_G(t) \rangle$ , *cf.* Eq. (6). However, it should be noted that the GDQC framework can be easily generalized to work with other local observables, including higher-order ones.

The proposed GDQC kernel function [*cf.* Eq. (1)] between two graphs,  $\mathcal{G}_\mu$  and  $\mathcal{G}_{\mu'}$ , is defined as scalar product,

$$\kappa_{\text{GDQC}}(\mathcal{G}_\mu, \mathcal{G}_{\mu'}) = \chi^\top [C^{\mathcal{G}_\mu}(t), D^{\mathcal{G}_\mu}] \chi [C^{\mathcal{G}_{\mu'}}(t), D^{\mathcal{G}_{\mu'}}]. \quad (13)$$

It involves a graph-dependent GDQC feature vector  $\chi[C^\mathcal{G}(t), D^\mathcal{G}]$  whose construction is the core element of the GDQC framework. Its construction is mathematically defined via algorithm 1, and it is illustrated in Fig. 2. It relies on binning procedures where separately the correlation matrix  $C_{i,j}^\mathcal{G}(t) \in [0, 1]$  and the distance matrix  $D_{i,j}^\mathcal{G}$  are binned. The former is binned into  $N_{\text{bins}}^C \geq 1$  intervals of size  $\Delta_C = 1/N_{\text{bins}}^C$  (bins associated with the upper axis in Fig. 2, while the latter is binned into  $N_{\text{bins}}^D \geq 1$  intervals of size  $\Delta_D = d_{\text{max}}/N_{\text{bins}}^D$  where  $d_{\text{max}}$  denotes the maximum distance across the entire dataset. In our case we work with graph distance (or the shortest-path distance), *i.e.* the distance measure  $d_G(i, j) \in \mathbb{N}$  is integer, which simplifies the process of distance binning. Here, the most natural choice is to use  $N_{\text{bins}}^D = d_{\text{max}} + 1$  bins, *i.e.* one bin for each value of graph distance (including distance 0) as illustrated on the lower axis in Fig. 2. Concerning the correlation binning we study the impact of the binning size  $\Delta_C = 1/N_{\text{bins}}^C$  in Subsec. IV A. The results

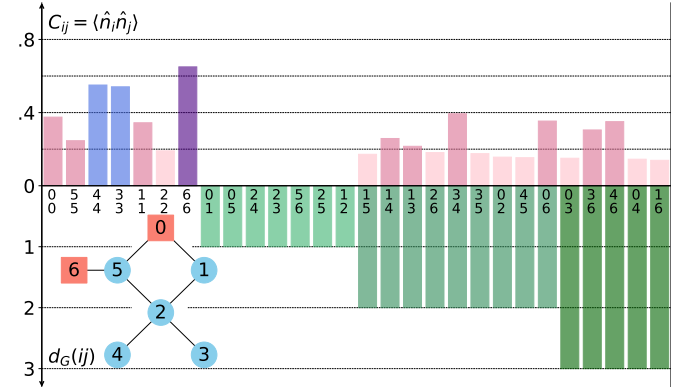


FIG. 2. Illustration for the construction of the generalized-distance quantum-correlation feature vector  $\chi[C^\mathcal{G}(t), D^\mathcal{G}]$  according to the algorithm 1 for the indicated graph. The figure shows for each pair of nodes  $(i, j)$  the measured correlation  $C_{i,j}^\mathcal{G}$  (upper bar) together with the respective distance measure  $d_G(i, j)$  (lower bar). Notice how the pairs that are at distance 1 showcase very low values due to the blockade phenomenon. Having chosen  $N_{\text{bins}}^C = 5$  correlation bins, the colors of the upper bars indicate which binning interval they are associated with. For example, there are 16 faint red values within the interval  $[0, 0.2]$ . Within the GDQC framework these values are further discriminated according to the graph distance between the involved nodes. Thus, the 16 faint red values are redistributed according to the four involved graph distance values, leading to a sequence  $\{1, 7, 5, 3\}$ . All bins combined, this procedure generates the  $(N_{\text{bins}}^C N_{\text{bins}}^D)$ -dimensional GDQC feature vector  $\chi$  which, in the present example becomes  $\chi = (1, 3, 2, 1, 0, 7, 0, 0, 0, 0, 5, 4, 0, 0, 0, 3, 2, 0, 0, 0)^\top / \sqrt{118}$ . The presented correlation matrix  $C_{i,j}^\mathcal{G} = C_{i,j}^\mathcal{G}(t = 1 \mu\text{s})$  corresponds to the emulation in Fig. 1.

presented in Sec. IV are derived for  $N_{\text{bins}}^C = 10$ . In combination the two binning procedures create the  $(N_{\text{bins}}^C N_{\text{bins}}^D)$ -dimensional GDQC feature vector  $\chi$  where each element is associated with a specific combination of correlation and distance bins. The value of each element is given as the count of correlation matrix elements  $C_{i,j}^\mathcal{G}(t)$  falling into the right value range, and whose involved nodes fall into the respective distance bin. In Fig. 2 we present a simple example of this binning procedure. In our study, similar to the protocol with the QEK algorithm [Subsec. III A], we test and compare the kernel function (13) for the two cases where the time evolution is either subjected to the global-detuning Hamiltonian  $\hat{\mathcal{H}}_{\text{glob}}^\mathcal{G}$  (9) or to the local-detuning one  $\hat{\mathcal{H}}_{\text{loc}}^\mathcal{G}$  (10). We denote the associated kernel functions as  $\kappa_{\text{GDQC}}^{\text{glob}}$  and  $\kappa_{\text{GDQC}}^{\text{loc}}$ , intended for non-attributed and attributed graphs, respectively.

**Proposition 2.** The kernel function  $\kappa_{\text{GDQC}}$  defined in Eq. (13) is: (1) A kernel function (symmetric positive semi-definite), (2) valid on graph data for any graph distance  $d_G$ , and (3) equal to 1 on any isomorphic pair  $\mathcal{G}_1$  and  $\mathcal{G}_2$ .

Next, we demonstrate that the GDQC kernel function  $\kappa_{\text{GDQC}}$  (13) satisfies all graph-kernel properties. Its key properties are summarized in proposition 2, and are proven in detail in App. B. Let us emphasize that the converse of point (3) is not proven to be true, *that is*, we do not claim that

$\kappa_{\text{GDQC}}(\mathcal{G}_1, \mathcal{G}_2) = 1$  if and only if  $\mathcal{G}_1$  and  $\mathcal{G}_2$  are isomorphic. A proof thereof (if it was true) would require a deeper analysis.

The similarity between the introduced GDQC kernel (13) and the Weisfeiler-Leman kernel [6], more precisely its generalized-distance Weisfeiler-and-Leman (GD-WL) version, can be made more explicit. To establish such a comparison, we first need to recall the notion of expressiveness in the context of kernel functions. Let  $\kappa_1$  and  $\kappa_2$  be two normalized graph kernels.

1. A graph kernel  $\kappa$  is expressive for a pair of two non-isomorphic graphs  $\mathcal{G}$  and  $\mathcal{G}'$  if  $\kappa(\mathcal{G}, \mathcal{G}') < 1$ .
2. A kernel  $\kappa_1$  is more expressive than a kernel  $\kappa_2$  if for any pair of non-isomorphic graphs,  $\mathcal{G}$  and  $\mathcal{G}'$ , two conditions are satisfied. First,  $\kappa_1(\mathcal{G}, \mathcal{G}') = 1$  always implies  $\kappa_2(\mathcal{G}, \mathcal{G}') = 1$ . Second, there exists at least one pair of non-isomorphic graphs,  $\mathcal{G}_*$  and  $\mathcal{G}'_*$ , such that  $\kappa_2(\mathcal{G}_*, \mathcal{G}'_*) = 1$  but  $\kappa_1(\mathcal{G}_*, \mathcal{G}'_*) < 1$ .

Here, a practical question concerns the choice of parameters that determine the lengths of the intervals  $\Delta_i^{(d)}$  and  $\Delta_i^{(q)}$ . Should one favor a larger or smaller number of bins? Intuitively, each approach has its advantages and drawbacks. The advantage comes mainly from the fact that increasing the number of bins increases the expressiveness of our kernels, which can be characterized by the following property:

**Proposition 3.** *The kernel function  $\kappa_{\text{GDQC}}$  is as expressive as the GD-WL test [37] given the latter is initialized with colors obtained from the multi-set of the values of the correlation matrix rows/columns.*

A proof of this proposition is provided in appendix C. One can also point out that if the selected graph distance is such that the corresponding GD-WL is less expressive than the quantum correlation matrix, then  $\kappa_{\text{GDQC}}$  expressiveness is upper bounded by the expressiveness of the quantum correlation matrix ( $QC$ ), as it already provides a stable coloring for the GD-WL (more details about GD-WL and its node coloring are to be found in Appendix C). This point is crucial, as the authors in [38] show that for several graph distances such as Laplacian eigenvectors, resistance distance and shortest path distance, GD-WL is upper bounded by 3-WL. On the other hand, the authors in [10] empirically show that the quantum correlation matrix of local observables issued from the Ising Hamiltonian is at least as powerful as 4-WL, as they are able to distinguish strongly regular graphs [39, 40]. When combined, these results provide empirical evidence that  $\kappa_{\text{GDQC}}$  is upper bounded by  $QC$  for the state-of-the-art graph distances studied in [38]. This suggests that computing  $\kappa_{\text{GDQC}}$  with "simple" graph distances (ex. shortest path distance) does not improve the kernel's expressiveness, but it does not necessarily suggest that it does not improve the performances of the subsequent machine learning model (cf. Sec. IV). Indeed, the main inconvenient for raising the number of bins (and thus improving the expressiveness) is that the corresponding Gram matrix would converge towards a binary matrix, which is not a suitable feature for kernel-based machine learning models. In fact, if one has a data set  $\mathcal{D}$  for which the kernel is fully expressive, and if

this dataset contains no isomorphic pair, then the Gram matrix would simply be the identity matrix, and one knows that such an input does not provide useful information for any machine learning model.

### C. Kernel pooling

In this part we describe a scheme that allows to combine information that comes from observables sampled at multiple time steps  $\{t_1, \dots, t_{N_t}\}$ , cf. Eq. (1). In principle, two qualitatively different strategies, i.e. two conceptually different functions  $F_\kappa$ , are conceivable. Either one feeds a large quantum-feature vector  $\mathcal{O}^{\mathcal{G}}$  comprising all time steps into a single kernel function, or one feeds all single-time-step quantum-feature vectors into separate kernel functions which are subsequently pooled. We proceed according to the second strategy, i.e. we generate a collection of  $N_t$  kernel functions  $\{\kappa_1, \dots, \kappa_{N_t}\}$ . Let  $f : \mathbb{R}^{N_t} \rightarrow \mathbb{R}$  be a function that preserves positive semi-definiteness (PSD), then by Mercer's theorem

$$\kappa(\mathcal{G}_1, \mathcal{G}_2) = f[\kappa_1(\mathcal{G}_1, \mathcal{G}_2), \dots, \kappa_{N_t}(\mathcal{G}_1, \mathcal{G}_2)], \quad (14)$$

the resulting expression  $\kappa(\mathcal{G}_1, \mathcal{G}_2)$  is also a valid kernel function. This includes polynomial kernels, exponential kernels and RBF-like kernels. In our case, we employ two pooling schemes: positive (convex) linear combinations defined by

$$\kappa_+(\mathcal{G}_1, \mathcal{G}_2) = \sum_{\gamma=1}^{N_t} \alpha_\gamma \kappa_\gamma(\mathcal{G}_1, \mathcal{G}_2) \quad (15)$$

where  $\sum_\gamma \alpha_\gamma = 1$ , and an element-wise product pooling defined by

$$\kappa_\times(\mathcal{G}_1, \mathcal{G}_2) = \prod_{\gamma=1}^{N_t} \kappa_\gamma(\mathcal{G}_1, \mathcal{G}_2). \quad (16)$$

From another perspective, this translates into the following : the feature map  $\chi(x)$  corresponding to the kernel  $\kappa$  can be expressed in terms of the feature maps  $\chi_i$  of the kernels  $\kappa_i$ . In the case of Eq. (15) we have :

$$\chi_+(\mathcal{G}) = \left\|_{\gamma=1}^{N_t} (\sqrt{\alpha_\gamma} \chi_\gamma(\mathcal{G})) \right\| \quad (17)$$

where  $\left\|_{\gamma=1}^{N_t}$  is the concatenation operator, and in the case of Eq. (16) we have

$$\chi_\times(\mathcal{G}) = \bigotimes_{\gamma=1}^{N_t} \chi_\gamma(\mathcal{G}) \quad (18)$$

where  $\bigotimes$  is the tensor product operator. This allows us to state the intuitive result formulated in proposition 4, see App. D for a detailed proof. It should be emphasized that according to proposition 4 it is possible that pooling improves the expressiveness, yet, it is not guaranteed. It depends on the expressiveness of the added kernels.

**Proposition 4.** *For a set  $S = \{\kappa_1, \kappa_2, \dots, \kappa_N\}$  of graph kernels, let  $\kappa_A$  and  $\kappa_B$  be respectively the kernels obtained from pooling two subsets  $S_A$  and  $S_B$  of  $S$ . If  $S_A \subset S_B$  then  $\kappa_A$  is at least as expressive as  $\kappa_B$ .*

TABLE I. Weighted F1 scores associated with the best-performing SVM models on two datasets, MUTAG\* and PTC\_FM\*, for various kernel implementations introduced in Sec. III: ranging from the classical kernels to the two quantum-feature kernels, QEK (12) and GDQC (13). The superscript (attr) on classical kernels denotes the incorporation of node features (attributes). The quantum-feature kernels are listed in a non-pooled and a pooled version where the subscript + ( $\times$ ) indicates sum- (Hadamard product-) pooling, cf. Subsec. IIIC. The superscripts (loc) and (glob) refer to whether the governing Hamiltonian has node features embedded [ $\hat{\mathcal{H}}_{\text{loc}}^{\mathcal{G}}$  (10)] or not [ $\hat{\mathcal{H}}_{\text{glob}}^{\mathcal{G}}$  (9)]. The **best**-, **second-to-best**, and **third-to-best** performing models are highlighted in the respective colors.

	Kernel	MUTAG* F1 score (%)	PTC_FM* F1 score (%)
Classical	Random Walk	84.37 $\pm$ 5.80	52.33 $\pm$ 4.17
	Subgraph sampling	81.70 $\pm$ 6.18	57.25 $\pm$ 4.55
	k-core	82.84 $\pm$ 5.24	59.10 $\pm$ 5.16
	Shortest path	80.72 $\pm$ 5.99	59.92 $\pm$ 4.97
	WL optimal assignment	84.64 $\pm$ 5.12	58.34 $\pm$ 5.10
	k-core <sup>(attr)</sup>	81.69 $\pm$ 6.13	59.10 $\pm$ 5.16
	Shortest path <sup>(attr)</sup>	80.00 $\pm$ 6.57	59.95 $\pm$ 4.64
	WL optimal assignment <sup>(attr)</sup>	86.10 $\pm$ 5.11	<b>64.96 <math>\pm</math> 5.18</b>
Quantum features	QEK <sup>(loc)</sup>	84.64 $\pm$ 5.05	60.87 $\pm$ 5.34
	QEK <sup>(glob)</sup>	84.57 $\pm$ 5.25	61.06 $\pm$ 5.37
	GDQC <sup>(loc)</sup>	86.78 $\pm$ 4.53	58.79 $\pm$ 5.39
	GDQC <sup>(glob)</sup>	86.09 $\pm$ 4.97	56.92 $\pm$ 4.79
	QEK <sup>(loc)</sup> <sub>+</sub>	87.08 $\pm$ 5.81	62.40 $\pm$ 5.77
	QEK <sup>(loc)</sup> <sub><math>\times</math></sub>	87.41 $\pm$ 6.20	<b>63.89 <math>\pm</math> 6.15</b>
	QEK <sup>(glob)</sup> <sub>+</sub>	86.33 $\pm$ 5.10	62.74 $\pm$ 5.12
	QEK <sup>(glob)</sup> <sub><math>\times</math></sub>	86.53 $\pm$ 4.80	62.42 $\pm$ 5.66
	GDQC <sup>(loc)</sup> <sub>+</sub>	<b>87.30 <math>\pm</math> 5.10</b>	62.18 $\pm$ 5.20
	GDQC <sup>(loc)</sup> <sub><math>\times</math></sub>	86.88 $\pm$ 4.90	<b>65.38 <math>\pm</math> 5.40</b>
	GDQC <sup>(glob)</sup> <sub>+</sub>	<b>88.06 <math>\pm</math> 5.00</b>	59.22 $\pm$ 5.80
	GDQC <sup>(glob)</sup> <sub><math>\times</math></sub>	<b>87.77 <math>\pm</math> 4.72</b>	60.33 $\pm$ 5.50

#### IV. RESULTS

In this section we present the extensive numerical results where we compare the various classical and quantum-feature kernel implementations introduced in Sec. III with respect to their prediction performance using a support vector machine (SVM). Table I summarizes the results, providing a full comparison across all models and their respective best performances.

We begin with a brief summary of the setup of the numerical experiment. For baseline purposes we pick five of the most widely used classical kernels [cf. Sec. III]: random walks, graphlets subsampling [41], k-core [34, 42], shortest path and Weisfeiler-Leman optimal assignment [43] kernels. Hereby, the last three methods can be implemented with and without supplied node features. In case node features are supplied we add the superscript (attr) to their name. The two quantum-feature kernels which are central to this study are the quantum evolution kernel (QEK) [Subsec. III A] which works with the global observable of the excitation probability  $P_k^{\mathcal{G}}(t)$  (6), and

the generalized-distance quantum-correlation (GDQC) kernel [Subsec. III B] which operates with the correlation matrix  $C_{i,j}^{\mathcal{G}}(t)$  (6), a local observables. A key element of this work lies in the elevation of the above quantum-feature kernels such that they can deal with attributed graphs. This is achieved through an implementation scheme where the atomic masses (the node features) are embedded into the local detuning of the Hamiltonian  $\hat{\mathcal{H}}_{\text{loc}}^{\mathcal{G}}$  (10), additional to the edge-embedding into the atomic positions, cf. Subsec. II B. In comparison we also evolve the quantum state under a global-detuning Hamiltonian  $\hat{\mathcal{H}}_{\text{glob}}^{\mathcal{G}}$  (9) where only the graph edges are embedded, but none of its node features. In Tabs. I-II and Fig. 3, depending on whether the observables that were forwarded to the QEK kernel (12) originate from a time evolution governed by  $\hat{\mathcal{H}}_{\text{loc}}^{\mathcal{G}}$  (10) or  $\hat{\mathcal{H}}_{\text{glob}}^{\mathcal{G}}$  (9) we denote the respective kernels as QEK<sup>(loc)</sup> or QEK<sup>(glob)</sup>, and analogously GDQC<sup>(loc)</sup> or GDQC<sup>(glob)</sup> for the GDQC kernel (13). Finally, we study the effect of kernel pooling where the information of observables sampled at different times is combined. The two implemented pooling schemes [cf. Subsec. III C] are sum-pooling (15) and element-wise product pooling (16). Accordingly, we add a subscript to the kernel names if pooling is applied: the subscript + for sum pooling and  $\times$  for product pooling, for example QEK<sup>(loc)</sup><sub>+</sub> or QEK<sup>(loc)</sup> <sub>$\times$</sub> , see Tabs. I-II.

Throughout this work the precomputed kernels are used to train a SVM on a classification task, see beginning of Sec. III for more details on kernel-based SVMs. The classification performance is evaluated using a weighted F1 score, a classification metric designed to address class imbalances in datasets such as in MUTAG\* and PTC\_FM\*. The weighted F1 score calculates the F1 score (the harmonic mean of precision and recall) for each class and then takes the weighted average based on the number of instances in each class. Here, we employ a repeated stratified 5-fold cross-validation with 10 repetitions, and we report the mean and standard deviation of the weighted F1 score across all cross-validation splits and repetitions. Furthermore, for every single kernel we perform a hyper-parameter tuning of the regularization parameter  $C$  of a SVM. We tune over 100 logarithmically spaced values in the interval  $C \in [0.001, 100]$ , and proceed with the best-performing SVM classifier. The computations involving the classical kernels conducted using the GraKel library [44]. The respectively best results are presented in Tab. I. Here, one notes that taking into account the node features generally improves the results. Moreover, the best performance is achieved by the WL optimal assignment kernel with supplied node features.

Next, we focus on the quantum-feature kernels. The observables are sampled at  $k = 20$  equally-spaced time steps  $\{t_1, t_2, \dots, t_k = t_{\text{max}}\}$  and respectively, two emulations (or time evolutions) are conducted, a shorter one with  $t_{\text{max}} = 1 \mu\text{s}$  and a longer one with  $t_{\text{max}} = 2 \mu\text{s}$ . We begin with non-pooled results. At each time step a quantum-feature kernel, QEK<sup>(loc/glob)</sup> or GDQC<sup>(loc/glob)</sup>, is precomputed and used to train a SVM. The resulting F1 scores for  $t_{\text{max}} = 1 \mu\text{s}$  and for both datasets, MUTAG\* and PTC\_FM\*, are presented in Fig. 3. Overall, both kernels, QEK and GDQC, yield comparative results; importantly, all results are significantly above the



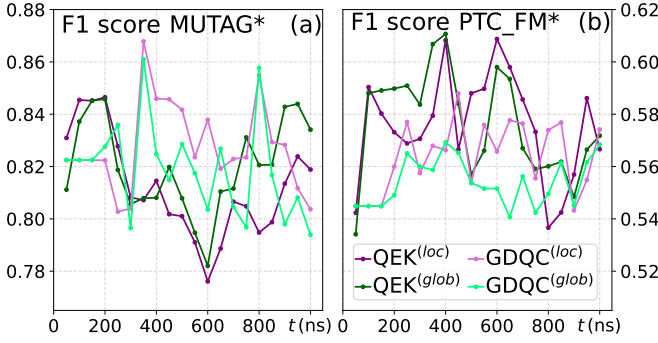


FIG. 3. Weighted F1 scores associated with SVMs trained on the quantum-feature kernels, QEK (12) and GDQC (13), for the two datasets, (a) MUTAG\* and (b) PTC\_FM\*. The superscripts (loc) and (glob) refer to whether the governing Hamiltonian has node features embedded [ $\hat{H}_{\text{loc}}^{\mathcal{G}}$  (10)] or not [ $\hat{H}_{\text{glob}}^{\mathcal{G}}$  (9)]. The training and evaluation procedure is separately conducted at each time steps across the time evolution. For comparison, the corresponding randomly stratified baseline, where each class is predicted proportionally to its frequency in the dataset are 0.55 for MUTAG and 0.51 for PTC\_FM, significantly below the presented F1 scores.

random baseline (black dashed line). In terms of the differences in using the node-feature embedded Hamiltonian  $\hat{H}_{\text{loc}}^{\mathcal{G}}$  [superscript (loc)] or the global-detuning Hamiltonian  $\hat{H}_{\text{glob}}^{\mathcal{G}}$  [superscript (glob)], no clear trend can be observed. As a function of the sampling time steps, the performances vary slightly within a range of  $\sim 5\%$  in F1 score. The maxima in the sequence, *i.e.* the best-performing models are added to Tab. I. Interestingly, for MUTAG\* the GDQC performance is on par with the best classical score whereas for PTC\_FM\* the QEK kernel has achieved a higher score than all classical models except for the WL optimal assignment<sup>(attr)</sup>.

Next, we employ pooling schemes in order to potentially further enhance the performance of the quantum-feature kernels. The two pooling scheme which we apply are described in Subsec. III C. However, the decision on which of the  $k = 20$  time steps to pool, and how many time steps to use is quite arbitrary. Instead of relying on a predetermined strategy, we fix the number of time steps to use, and randomly select 1000 tuples of time-steps combinations. The goal of this study is really to comprehend by how much the performance of our models can be enhanced by means of information pooling. For this reason, we only report the best-performing models for each tuple size.

Having chosen the tuple sizes to 3 and 5, we show the best-performing models for  $t_{\text{max}} = 1\mu\text{s}$  and  $t_{\text{max}} = 2\mu\text{s}$  in Tab. II. For each model we list the involved pooled time steps. The first thing to notice is that pooling can significantly enhance the model performance. With the best-performing pooling models from each kernel class added to Tab. I we achieve an F1-score increase by  $\sim 2\%$  on the MUTAG\* dataset and by  $\sim 4\%$  for PTC\_FM\*. As a result, we find the best-performing quantum-feature models outperforming the classical algorithms. Considering the results in Tabs. I-II one notices a fairly common trend which is a high F1 score on one of the datasets, MUTAG\* or PTC\_FM\*, being accompanied by a

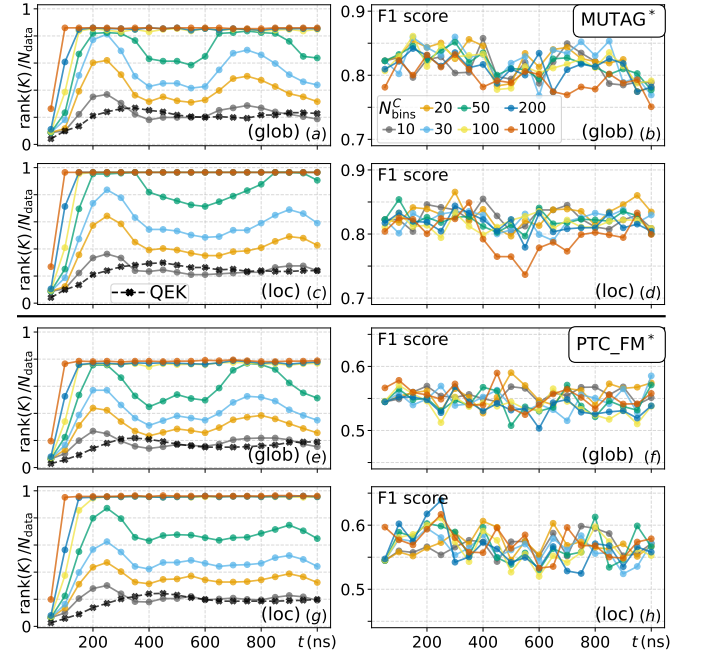


FIG. 4. Relative rank of the Gram matrix  $\text{rank}(K)/N_{\text{data}}$  associated with the GDQC kernel  $\kappa_{\text{GDQC}}$  (13) versus the F1 score of the corresponding kernel-based SVM for varying binning number  $N_{\text{bins}}^C$ . The quantities are plotted as a function of the time steps across the entire time evolution with  $t_{\text{max}} = 1\mu\text{s}$ . (a)-(d) corresponds to the dataset MUTAG\*; (e)-(h) corresponds to PTC\_FM\*. The identifier (loc) [(glob)] imply that the involved time evolution is governed by the Hamiltonian  $\hat{H}_{\text{loc}}^{\mathcal{G}}$  (10) [ $\hat{H}_{\text{glob}}^{\mathcal{G}}$  (9)], whereby  $\hat{H}_{\text{loc}}^{\mathcal{G}}$  has node features embedded. For comparison, the black dashed line with x-markers represents the relative rank associated with the QEK kernel  $\kappa_{\text{QEK}}$  (12), which does not depend on binning.

low score on the other dataset. This is particularly pronounced for the classical random walk and shortest-distance kernels. Similarly,  $\text{GDQC}_{+}^{(\text{glob})}$  achieves the highest F1 scores on the MUTAG\* dataset across all models, but it scores among the lowest on PTC\_FM\*, see Tab. II. Albeit not being statistically significant, in Tab. II we find 5 out of the top 6 best-performing models associated with the GDQC kernel, maybe hinting at a potential edge of GDQC over the QEK kernel.

### A. Binning-size dependence of GDQC

In this part we study the impact of the chosen binning size  $\Delta_C = 1/N_{\text{bins}}^C$  which is applied to the correlation matrix  $C_{i,j}^{\mathcal{G}}(t)$  within the GDQC framework, *cf.* Subsec. III B.

For this purpose, we vary the number of bins  $N_{\text{bins}}^C$  and we study two quantities providing complementary information. First, we compute the F1 score showcasing the actual performance of the respective GDQC model. Second, we compare it with the rank of the Gram matrix  $K$  where  $K_{\mu,\mu'} = \kappa_{\text{GDQC}}(\mathcal{G}_{\mu}, \mathcal{G}_{\mu'})$  with  $\mu, \mu' \in \{1, 2, \dots, N_{\text{data}}\}$  and the size of the dataset  $N_{\text{data}}$ . The rank of a matrix indicates how many of its constituent vectors are linearly independent.

TABLE II. Weighted F1 scores associated with SVMs trained on different pooled quantum-feature kernel implementations. The notation is identical to Tab. I. Shown are the best-performing models with pooling over 3-tuples and 5-tuples of time steps, for the two sets of sampled times with  $t_{\max} = 1 \mu\text{s}$  and  $t_{\max} = 2 \mu\text{s}$ . The respective pooled time steps are included in the table. The best-performing model for each kernel type is added to Tab. I.

	Kernel	MUTAG*		PTC_FM*	
		time steps ( $\mu\text{s}$ )	F1 Score (%)	time steps ( $\mu\text{s}$ )	F1 Score (%)
maximum evolution time: $t_{\max} = 1 \mu\text{s}$	QEK $_{\times}^{(\text{loc})}$	{0.2, 0.75, 0.95} {0.15, 0.25, 0.4, 0.65, 0.95}	86.75 $\pm$ 5.67 87.41 $\pm$ 6.2	{0.1, 0.4, 0.9} {0.05, 0.2, 0.4, 0.5, 0.95}	63.33 $\pm$ 5.90 <b>63.89 <math>\pm</math> 6.15</b>
	QEK $_{+}^{(\text{loc})}$	{0.2, 0.75, 0.9} {0.05, 0.1, 0.25, 0.75, 0.9}	87.08 $\pm$ 5.81 86.80 $\pm$ 5.53	{0.2, 0.7, 0.95} {0.25, 0.4, 0.7, 0.95, 1.}	62.40 $\pm$ 5.77 62.35 $\pm$ 5.70
	QEK $_{\times}^{(\text{glob})}$	{0.05 0.15 0.2} {0.1 0.25 0.8 0.85 0.9}	85.7 $\pm$ 5.44 85.01 $\pm$ 6.2	{0.05 0.35 0.4} {0.05 0.1 0.2 0.35 0.4}	62.42 $\pm$ 5.66 60.77 $\pm$ 6.02
	QEK $_{+}^{(\text{glob})}$	{0.1 0.2 0.8} {0.05 0.1 0.2 0.8 0.85}	84.98 $\pm$ 5.71 84.96 $\pm$ 5.47	{0.2 0.35 0.4} {0.05 0.2 0.25 0.35 0.4}	62.74 $\pm$ 5.12 61.48 $\pm$ 5.13
	GDQC $_{\times}^{(\text{loc})}$	{0.05 0.15 0.8} {0.05 0.1 0.15 0.25 0.35}	85.92 $\pm$ 5.95 85.29 $\pm$ 5.57	{0.45 0.5 0.9} {0.3 0.45 0.5 0.55 0.9}	62.98 $\pm$ 5.31 <b>63.71 <math>\pm</math> 5.26</b>
	GDQC $_{+}^{(\text{loc})}$	{0.1 0.35 0.8} {0.1 0.35 0.8 0.85 0.9}	86.49 $\pm$ 5.22 86.0 $\pm$ 5.67	{0.25 0.35 0.45} {0.1 0.25 0.35 0.55 0.85}	61.96 $\pm$ 5.87 61.83 $\pm$ 5.55
	GDQC $_{\times}^{(\text{glob})}$	{0.1 0.35 0.8} {0.05 0.15 0.2 0.35 0.8}	<b>87.77 <math>\pm</math> 4.72</b> 87.06 $\pm$ 5.18	{0.05 0.25 0.45} {0.15 0.25 0.45 0.6 0.9}	59.73 $\pm$ 5.54 59.07 $\pm$ 5.32
	GDQC $_{+}^{(\text{glob})}$	{0.35 0.65 0.8} {0.05 0.25 0.55 0.8 0.95}	<b>88.06 <math>\pm</math> 5.0</b> <b>88.0 <math>\pm</math> 5.1</b>	{0.7 0.95 1.0} {0.15 0.6 0.7 0.95 1.0}	57.96 $\pm$ 4.4 58.08 $\pm$ 5.1
maximum evolution time: $t_{\max} = 2 \mu\text{s}$	QEK $_{\times}^{(\text{loc})}$	{0.2 1.2 1.6} {0.2 0.3 0.5 1.2 1.6}	86.83 $\pm$ 5.6 86.26 $\pm$ 5.6	{0.1 0.4 1.0} {0.2 0.4 0.7 1.0 1.1}	63.12 $\pm$ 6.0 63.17 $\pm$ 5.5
	QEK $_{+}^{(\text{loc})}$	{0.2 0.6 0.9} {0.2 0.3 0.7 1.2 1.6}	85.8 $\pm$ 5.9 85.67 $\pm$ 5.8	{0.3 1.3 1.8} {0.3 1.3 1.7 1.8 1.9}	62.29 $\pm$ 5.9 62.26 $\pm$ 5.9
	QEK $_{\times}^{(\text{glob})}$	{0.1 0.2 1.5} {0.1, 0.2, 1.3, 1.5, 2.0}	86.53 $\pm$ 4.8 86.05 $\pm$ 5.16	{0.3 1.5 1.6} {0.4 1.4 1.5 1.6 1.8}	61.76 $\pm$ 4.9 61.94 $\pm$ 5.5
	QEK $_{+}^{(\text{glob})}$	{0.2 1.5 2.0} {0.2 0.8 1.3 1.5 1.7}	86.33 $\pm$ 5.1 85.68 $\pm$ 5.5	{0.3 1.5 1.6} {0.2 0.3 1.3 1.4 1.5}	61.2 $\pm$ 5.1 61.99 $\pm$ 5.0
	GDQC $_{\times}^{(\text{loc})}$	{0.1 0.8 1.4} {0.5 0.8 1.1 1.2 1.5}	86.82 $\pm$ 5.6 86.88 $\pm$ 4.9	{0.5 1.3 1.6} {0.4 0.5 0.9 1.1 1.6}	62.87 $\pm$ 6.0 <b>65.38 <math>\pm</math> 5.4</b>
	GDQC $_{+}^{(\text{loc})}$	{0.6 0.8 1.4} {0.2 0.8 1.1 1.2 1.4}	86.78 $\pm$ 5.2 87.3 $\pm$ 5.1	{1.3 1.6 1.7} {0.5 0.8 1.3 1.6 1.7}	61.04 $\pm$ 5.7 62.18 $\pm$ 5.2
	GDQC $_{\times}^{(\text{glob})}$	{0.3 0.8 1.3} {0.1 0.7 0.8 1.2 1.3}	87.11 $\pm$ 4.9 87.32 $\pm$ 5.0	{1.0 1.3 1.6} {0.1 0.2 0.6 1.0 1.6}	60.33 $\pm$ 5.5 58.86 $\pm$ 5.2
	GDQC $_{+}^{(\text{glob})}$	{0.5 0.7 0.8} {0.3 0.5 0.8 1.3 1.6}	86.51 $\pm$ 5.2 87.18 $\pm$ 5.1	{0.8 1.6 1.8} {0.2 0.8 1.3 1.6 1.8}	59.12 $\pm$ 5.0 59.22 $\pm$ 5.8

As such the rank of the Gram matrix  $\text{rank}(K)$  provides insights into the expressiveness of the kernel; the more linearly-independent GDQC feature vectors  $\chi[C^{\mathcal{G}_{\mu}}(t), D^{\mathcal{G}_{\mu}}]$ , the more expressive the kernel. The two quantities, the relative rank  $\text{rank}(K)/N_{\text{data}}$  and the F1 score, are plotted in Fig. 4 for varying number of bins  $N_{\text{bins}}^C$  and across the entire time evolution with  $t_{\max} = 1 \mu\text{s}$ .

The first thing to note is that increasing the number of bins  $N_{\text{bins}}^C$  does improve the expressiveness of the GDQC kernel  $\kappa_{\text{GDQC}}^C$  (13) as the rank of the Gram matrix increases significantly. Beyond a certain number of bins, the relative rank saturates. Interestingly, the saturation for the local-detuning case GDQC $^{(\text{loc})}$  reaches almost 1 [panels (c),(g)] whereas the

global-detuning case GDQC $^{(\text{glob})}$  saturates at a smaller value [panels (a),(e)]. This difference can be traced back to the qualitative difference between both kernel implementations: the local-detuning kernel being more expressive. In this particular case, there are molecules in the datasets which share the same atomic placements (the non-attributed underlying graph) but whose atomic constituents (the node features) are different. The local-detuning kernel  $\kappa_{\text{GDQC}}^{\text{loc}}$  is able to differentiate such molecules whereas the global-detuning kernel  $\kappa_{\text{GDQC}}^{\text{glob}}$  is not, resulting in a lower Gram-matrix rank for the latter. The tiny difference between 1 and the local-detuning plateaus in panels (c) and (g) can be traced back to a few molecules which only differ by the presence of hydrogen atoms—which are omitted

in the embedded graphs. The second main observation is that increasing the expressiveness of the kernel does not increase the performances of the SVM model. Indeed in both data sets, the F1 score is comparable when computing the  $\kappa_{\text{GDQC}}$  with  $N_{\text{bins}}^C = 10$  and with  $N_{\text{bins}}^C = 1000$ , even when the rank of the Gram matrix is 4 times larger.

At last we compare the expressiveness of the two quantum-feature kernels studied in this work, the GDQC kernel  $\kappa_{\text{GDQC}}$  (13) and the QEK kernel  $\kappa_{\text{QEK}}$  (12). To this end, we added the rank of the Gram matrix associated with QEK to Figs. 4(a),(c),(e),(g), shown as the black dashed line with x markers. Recall that there is no binning dependence in the QEK algorithm. Interestingly, the rank of  $\kappa_{\text{QEK}}$  is as low as it is for  $\kappa_{\text{GDQC}}$  with only  $N_{\text{bins}}^C = 10$ . One conjecture is that the proposed GDQC kernel can be chosen such that its expressiveness is significantly larger compared than what it is for the QEK kernel. Nonetheless, regardless the expressiveness the corresponding F1 scores are very similar, cf. Fig. 3. This finding supports the hypothesis that the performance of a kernel-based machine learning model is not only influenced by the expressiveness of the involved kernel, but also by its capacity to associate the relevant "similarity scores" to the corresponding data points.

## V. CONCLUSION AND PERSPECTIVES

In this work, we explore different quantum-feature kernel implementations (1) and we study their performances on two benchmark datasets using a support vector machine (SVM). In a first step we introduce a graph-embedding scheme that not only allows for the edge features to be embedded in a neutral-atom Rydberg Hamiltonian (2), but also for the node features (the atomic masses) via an appropriate choice of the local detuning fields, cf. Subsec. II B. Hence, we study the effect of node-feature embedding [time evolution via  $\hat{\mathcal{H}}_{\text{loc}}^{\mathcal{G}}$  (10)] versus non-node-feature embedding [time evolution via  $\hat{\mathcal{H}}_{\text{glob}}^{\mathcal{G}}$  (9)]. Having demonstrated theoretically (cf. proposition 1) and empirically (cf. Fig. 4) that node-feature embedding enhances the kernel's expressiveness, we observe a comparable SVM-prediction performance between the two cases (cf. Fig. 3).

In a second step, we compare two conceptually different quantum-feature kernels: the quantum evolution kernel (QEK)  $\kappa_{\text{QEK}}$  (12) [13, 14] which operates with a global observable, the excitation probability  $P_k^{\mathcal{G}}$  (6), and the proposed generalized-distance quantum-correlation (GDQC) kernel  $\kappa_{\text{GDQC}}$  (13) which draws from the correlation matrix  $C_{i,j}^{\mathcal{G}}$  (6), a local observable. While these two kernels could perform qualitatively different for different graph-related prediction tasks, for the global prediction task studied in this work, both kernels lead to a comparable performance which is on par with standard classical state-of-the-art algorithms (cf. Tab. I).

In a third step, we attempt to further enhance the quantum-feature kernels' performance. For this purpose we combine the information of observables sampled at multiple steps across the time evolution by means of pooling operations (cf. Subsec. III C). Here, we find that pooling can significantly enhance the models performance enabling the quantum-feature kernels

to surpass the classical baselines (cf. Tabs. I-II). Together, the presented quantum-feature kernel implementations enlarge the scope of the previously existing techniques in the field of quantum graph machine learning.

Hyper-parameter sensitivity remains an open question. We notice that it is difficult to draw definitive conclusions on the global tendencies of our models depending on parameter choices, such as the local detuning value  $\delta_0$  [cf. Eq. (8)], the Rabi frequency  $\Omega$  [cf. Eq. (2)], as well as the time steps at which to sample the observables (regardless whether they are pooled or not). This motivates the need of automatic, data-driven strategies to set these hyper-parameters such as gradient-based optimization, Bayesian- or evolutionary search.

## ACKNOWLEDGMENTS

The author gratefully acknowledges Louis-Paul Henry, Vittorio Vitale, and Francesco Musso for the many fruitful discussions that have significantly contributed to the development of this work. We would also like to thank Anton Quelle, Kemal Bidzhiev, Mauro Mendizabal, and Elie Merhej for their valuable contributions to the development of the emulation tools, which were essential for the implementation of the algorithms presented in this work.

### Appendix A: Improved graph discrimination using local detuning

In this Appendix we demonstrate the claim of proposition 1 in the main text: A quantum evolution kernel  $\kappa_{\text{loc}}^{\mathcal{G}}(\mathcal{G}_{\mu}, \mathcal{G}_{\mu'})$  derived from a local-detuning Hamiltonian  $\hat{\mathcal{H}}_{\text{loc}}^{\mathcal{G}}$  (10) is genuinely more expressive than its counterpart  $\kappa_{\text{glob}}^{\mathcal{G}}(\mathcal{G}_{\mu}, \mathcal{G}_{\mu'})$  derived from the global-detuning Hamiltonian  $\hat{\mathcal{H}}_{\text{glob}}^{\mathcal{G}}$  (9) for distinguishing attributed graphs.

This proposition is demonstrated in two steps. (i) We show that there exist non-isomorphic graphs which can be distinguished by the local kernel, i.e.  $\kappa_{\text{loc}}^{\mathcal{G}}(\mathcal{G}_{\mu}, \mathcal{G}_{\mu'}) \neq 0$ , but not by the global counterpart, i.e.  $\kappa_{\text{glob}}^{\mathcal{G}}(\mathcal{G}_{\mu}, \mathcal{G}_{\mu'}) = 0$ . (ii) We show that the converse is always given in general, i.e. if the global kernel is able to distinguish two non-isomorphic graphs [ $\kappa_{\text{glob}}^{\mathcal{G}}(\mathcal{G}_{\mu}, \mathcal{G}_{\mu'}) \neq 0$ ], then the local kernel is able to do the same [ $\kappa_{\text{loc}}^{\mathcal{G}}(\mathcal{G}_{\mu}, \mathcal{G}_{\mu'}) \neq 0$ ]. Here, the term *in general* implies that accidental choices of specific detuning values causing the local kernel to vanish can never be ruled out. We argue however, that such accidental zeros form a lower-dimensional manifold in parameter space and are thus non-generic. In practical terms, it implies that a given (non-fine-tuned) choice of local detuning values will almost surely avoid the accidental manifold.

(i) Here, it is sufficient to present one pair of non-isomorphic graphs which satisfy the requirement, i.e. the local kernel can distinguish them but the global one can not. This situation arises for any two graphs which have identical edges (and node positions) but different node features. Since the local kernel encodes node features it would be able to distinguish such graphs whereas for the global kernel the two graphs are

indistinguishable. In the context of the studied molecules the node features that were associated with the local detuning field were the atomic masses, *cf.* Eq. (8). One example could be two molecules with identical (or nearly identical) atomic positions, but consisting of different atoms, such as nitrogen monoxide NO [ $a_{\text{NO}} = 115$  pm] and carbon monoxide CO [ $a_{\text{CO}} = 113$  pm]. The bond distance is negligible but the atomic masses,  $m_{\text{N}} = 14.01$  u and  $m_{\text{C}} = 12.01$  u, allow for a robust distinction.

(ii) In order to demonstrate the second point, we first recall some notation. We start from the general quantum evolution kernel Eq. (1),

$$K_{\mu\mu'} = F_{\kappa} [\mathcal{O}^{\mathcal{G}_{\mu}}(\mathbb{J}^{\mathcal{G}_{\mu}}, \Omega, \delta), \mathcal{O}^{\mathcal{G}_{\mu'}}(\mathbb{J}^{\mathcal{G}_{\mu'}}, \Omega, \delta')]. \quad (\text{A1})$$

For convenience, we define the observable vectors  $\mathcal{O}^{\mathcal{G}_{\mu}}(\mathbb{J}^{\mathcal{G}_{\mu}}, \Omega, \delta)$  as functions of Hamiltonian parameters (2) depending on which Hamiltonian they were subjected to, *cf.* Eqs. (9), and (10). This allows us to define the function

$$F(\delta^{\text{tot}}) = F_{\kappa} [\mathcal{O}^{\mathcal{G}_{\mu}}(\mathbb{J}^{\mathcal{G}_{\mu}}, \Omega, \delta), \mathcal{O}^{\mathcal{G}_{\mu'}}(\mathbb{J}^{\mathcal{G}_{\mu'}}, \Omega, \delta')], \quad (\text{A2})$$

which exclusively depends on the local detuning with the  $d_{\text{max}}^{\text{tot}}$ -dimensional vector  $\delta^{\text{tot}} = (\delta, \delta')$  and  $d_{\text{max}}^{\text{tot}} = |\mathcal{V}| + |\mathcal{V}'|$ . The function  $F(\delta^{\text{tot}})$  is defined on the domain  $\Gamma := \{\delta^{\text{tot}} \in \mathbb{R}^{d_{\text{max}}^{\text{tot}}}\}$ . Similarly as in the global-detuning Hamiltonian (9), we define the total global detuning vector as  $\delta_{\text{glob}}^{\text{tot}} = (\delta_0, \dots, \delta_0)$ . Now, we can recast the initial assumption wherein the global kernel is able to distinguish the two non-isomorphic graphs as

$$F(\delta_{\text{glob}}^{\text{tot}}) \neq 0. \quad (\text{A3})$$

At this state we employ the identity theorem. Let us assume that  $F_{\kappa}$  is a real-analytic function and the same is the case for any observable  $\mathcal{O}^{\mathcal{G}_{\mu}}(\mathbb{J}^{\mathcal{G}_{\mu}}, \Omega, \delta)$ ; the latter is discussed at the end of this Appendix. Given these assumptions, it follows that the function  $F(\delta^{\text{tot}})$  [Eq. (A2)] is also real-analytic on the entire domain  $\Gamma$ , and thus, the identity theorem is applicable. We use a proof by contradiction. Let us assume that there exists an open set on the domain  $\Gamma$  (*i.e.* a manifold with full dimension  $d_{\text{max}}^{\text{tot}}$ ) on which  $F(\delta^{\text{tot}}) = 0$ . The identity theorem would then require that  $F(\delta^{\text{tot}}) = 0$  on the entire domain  $\Gamma$ . This, however, contradicts Eq. (A3) since  $\delta_{\text{glob}}^{\text{tot}}$  lies within the domain. As a result, no such open sets can exist on the domain  $\Gamma$ . Manifolds on which the function  $F(\delta^{\text{tot}})$  vanishes are at most of dimension  $d_{\text{max}}^{\text{tot}} - 1$ . This circumstance makes it very unlikely that a generic choice of detuning parameters fall onto such a manifold.

Lastly, we discuss the analyticity of observables  $O(t, \lambda) = \langle \psi(t, \lambda) | \hat{O} | \psi(t, \lambda) \rangle$  dependent on time  $t$  and Hamiltonian parameters  $\lambda$ , in our case  $\lambda = (\mathbb{J}, \Omega, \delta)$ . Under fairly general assumptions, if the Hamiltonian  $\hat{\mathcal{H}}(t, \lambda)$  and the initial state  $|\psi(0, \lambda)\rangle$  depend analytically on parameters  $\lambda$ , then the time-evolved state  $|\psi(t, \lambda)\rangle = \hat{U}(t, \lambda) |\psi(0, \lambda)\rangle$  and all standard observable expectation values are also real-analytic functions of  $\lambda$  [45, 46]. Here,  $\hat{U}(t, \lambda)$  is the time-evolution operator.

The question is really in which cases could the observable be non-analytic. In the following we break down 5 possibilities where it could occur, and argue that none of these scenarios apply to our case.

(1) Undoubtedly, if either the Hamiltonian  $\hat{\mathcal{H}}(t, \lambda)$  or the initial state  $|\psi(0, \lambda)\rangle$  depend non-analytically on the parameters, the non-analyticity would be propagated to any observable. For example, an initial state could be prepared as a ground state of  $\hat{\mathcal{H}}(0, \lambda)$ , and be non-analytically due to a level crossing. In our setup, neither is the case. The Hamiltonian is a smooth function of its parameters, and the initial state is quite featureless; it is the all-zero state  $|\psi(0, \lambda)\rangle = |0\rangle$ .

(2) Non-analytic behavior is encountered in the context of phase transitions: order-parameter kinks, and jumps, etc.. Such non-analyticities appear across the whole phase transition spectrum: thermal transitions, quantum phase transitions, dynamical phase transitions, topological phase transitions, or even many-body localization (MBL) transitions, regardless whether they are classified as first-order or second-order transitions. Nonetheless, true non-analyticities only appear in the thermodynamic limit (for infinitely large system sizes). For finite-size systems, such as the graphs which we are interested in, no non-analytic behavior is caused by phase transitions. All quantities are analytic and evolve smoothly across potential transition regions.

(3) Non-analytic behavior can also appear inside a MBL phase (additionally to the transition boundary non-analyticities) or within certain glassy systems. Again, these features are only genuinely non-analytic in the thermodynamic limit.

(4) Non-standard observables such as post-selected observables could also cause non-analytic behavior. In the context of post-selected observables, the time-evolved state is first projected onto a specific subspace of the Hilbert space before an observable operator is applied. This can trigger a non-analytic behavior, for example if the state has zero weight in the respective subspace, leading to a divergence due to the normalization. In the presented protocol, only standard observables are implemented, see Eq. (6).

(5) Non-analyticities can also appear in the context of level crossings. Here, however, they only show for specific observables. For example, if one tracks an observable for a specific eigenstate (such as the ground state). For our implemented observables, level crossings do not cause non-analytic behavior.

## Appendix B: Properties of GDQC

In this appendix we prove the proposition 2: *The kernel function  $\kappa_{\text{GDQC}}$  defined Eq. (13) is: (1) a kernel function (symmetric positive semi-definite), (2) valid on graph data for any graph distance  $d_G$ , and (3) equal to 1 on any isomorphic pair  $\mathcal{G}_1$  and  $\mathcal{G}_2$ .*

Let us recall that the generalized-distance quantum-correlation kernel (GDQC)  $\kappa_{\text{GDQC}}$  (13) is defined via a scalar



product

$$\begin{aligned} K_{\mu\mu'}^{\text{GDQC}} &= \kappa_{\text{GDQC}}(\mathcal{G}_\mu, \mathcal{G}_{\mu'}) \\ &= \chi^\top [C^{\mathcal{G}_\mu}(t), D^{\mathcal{G}_\mu}] \chi [C^{\mathcal{G}_{\mu'}}(t), D^{\mathcal{G}_{\mu'}}] \\ &= \sum_{\nu=1}^{N_\chi} \chi_\nu [C^{\mathcal{G}_\mu}(t), D^{\mathcal{G}_\mu}] \chi_\nu [C^{\mathcal{G}_{\mu'}}(t), D^{\mathcal{G}_{\mu'}}], \end{aligned} \quad (\text{B1})$$

where  $C^{\mathcal{G}}(t)$  denotes the correlation matrix (6) associated with the graph  $\mathcal{G}$ , cf. Eqs. (1), (9), (10), and  $D^{\mathcal{G}}$  is the generalized-distance matrix. The index iterates over the whole dataset of  $N_{\text{data}}$  graphs, i.e.  $\mu, \mu' \in \{1, 2, \dots, N_{\text{data}}\}$ . Naturally, the correlation matrix  $C^{\mathcal{G}}(t)$  is a real-valued observable since it is derived from a Hermitian operator. Consequently, each element of the  $N_\chi$ -dimensional GDQC feature vector  $\chi [C^{\mathcal{G}}(t), D^{\mathcal{G}}]$  is real-valued with  $N_\chi = N_{\text{bins}}^C N_{\text{bins}}^D$ . By continuation, the GDQC kernel  $\kappa_{\text{GDQC}}(\mathcal{G}_\mu, \mathcal{G}_{\mu'})$  is also real-valued. Next, we prove the 3 statements of proposition 2 point by point.

*Proof.* (1) A kernel defined via a scalar product like  $\kappa_{\text{GDQC}}$  (B1) is symmetric, i.e.  $\kappa_{\text{GDQC}}(\mathcal{G}_\mu, \mathcal{G}_{\mu'}) = \kappa_{\text{GDQC}}(\mathcal{G}_{\mu'}, \mathcal{G}_\mu)$ . Moreover, a kernel is positive semi-definite if for any real vector  $\mathbf{c} \in \mathbb{R}^{N_{\text{data}}}$  it holds  $\mathbf{c}^\top K^{\text{GDQC}} \mathbf{c} \geq 0$ . An explicit computation directly leads to

$$\mathbf{c}^\top K^{\text{GDQC}} \mathbf{c} = \sum_{\nu=1}^{N_\chi} \left( \sum_{\mu} c_\mu \chi_\nu [C^{\mathcal{G}_\mu}(t), D^{\mathcal{G}_\mu}] \right)^2 \geq 0, \quad (\text{B2})$$

confirming that the GDQC kernel is indeed positive semi-definite.

(2). We demonstrate that the kernel is invariant under node label permutations. Hereby, it suffices to show that the GDQC feature vector satisfies

$$\chi [C^{\mathcal{G}^\Pi}(t), D^{\mathcal{G}^\Pi}] = \chi [C^{\mathcal{G}}(t), D^{\mathcal{G}}], \quad (\text{B3})$$

with  $\mathcal{G}^\Pi$  being a graph which has its nodes permuted by a given permutation  $\Pi$ . Specifically, we demonstrate that the correlation and distance matrices of a permuted graph are related to their non-permuted counterparts via the relations

$$C_{i,j}^{\mathcal{G}^\Pi} = C_{\Pi^{-1}(i), \Pi^{-1}(j)}^{\mathcal{G}}, \quad D_{i,j}^{\mathcal{G}^\Pi} = D_{\Pi^{-1}(i), \Pi^{-1}(j)}^{\mathcal{G}}. \quad (\text{B4})$$

Consequently, the permutation of a graph is identical to the inverse permutation of the matrix indices associated with the non-permuted graph. Such a transformation, however, has no effect on the GDQC feature vector  $\chi [C^{\mathcal{G}}(t), D^{\mathcal{G}}]$ , as the feature-vector elements are simply counts of the number of values falling into a predefined interval, cf. algorithm 1 and Fig. 2. Thus, the GDQC kernel  $\kappa_{\text{GDQC}}$  (B1) is invariant under node label permutations. It remains to prove that the transformation relations (B4) are actually true.

Concerning the distances it is clear that the distance matrices associated with  $\mathcal{G}$  and  $\mathcal{G}^\Pi$  are related via  $D_{i,j}^{\mathcal{G}} = D_{\Pi(i), \Pi(j)}^{\mathcal{G}^\Pi}$  leading to the relation in Eq. (B4). Concerning the correlation

matrix relation, a few mathematical steps are in order. We begin by considering the graph-embedded coupling matrix  $\mathbb{J}^{\mathcal{G}}$ , Eq. (7), and the local detuning field  $\delta^{\mathcal{G}}$ , Eq. (8). One directly obtains the relations

$$\mathbb{J}_{i,j}^{\mathcal{G}^\Pi} = \mathbb{J}_{\Pi^{-1}(i), \Pi^{-1}(j)}^{\mathcal{G}}, \quad \delta_i^{\mathcal{G}^\Pi} = \delta_{\Pi^{-1}(i)}^{\mathcal{G}}, \quad (\text{B5})$$

connecting the quantities between the permuted and the non-permuted graphs. Note that the relation (B5) for the detuning is also trivially satisfied for the global detuning case. Next, we define the unitary operator  $\hat{U}_\Pi$  which permutes the atoms according to  $\Pi$ . Its action on a basis state  $|\mathbf{b}\rangle$  is given by

$$\hat{U}_\Pi |\mathbf{b}\rangle = \hat{U}_\Pi |b_1 b_2 \dots b_N\rangle = |b_{\Pi(1)} b_{\Pi(2)} \dots b_{\Pi(N)}\rangle, \quad (\text{B6})$$

and hence, it transforms the local operators in the Hamiltonian [Eq. (2)] according to

$$\hat{U}_\Pi \hat{n}_i \hat{U}_\Pi^\dagger = \hat{n}_{\Pi(i)}, \quad \hat{U}_\Pi \hat{\sigma}_i^x \hat{U}_\Pi^\dagger = \hat{\sigma}_{\Pi(i)}^x. \quad (\text{B7})$$

Combining the properties (B5) and (B7), we obtain the Hamiltonian [Eq. (2)] relation

$$\hat{\mathcal{H}}(\mathbb{J}^{\mathcal{G}^\Pi}, \Omega, \delta^{\mathcal{G}^\Pi}) = \hat{U}_\Pi \hat{\mathcal{H}}(\mathbb{J}^{\mathcal{G}}, \Omega, \delta^{\mathcal{G}}) \hat{U}_\Pi^\dagger, \quad (\text{B8})$$

where in between we switched the summation indices  $i \rightarrow i' = \Pi^{-1}(i)$  before applying Eq. (B7). Correspondingly, the time-evolved state (5),

$$|\psi_{\mathcal{G}}(t)\rangle = \exp[-i(t/\hbar) \hat{\mathcal{H}}(\mathbb{J}^{\mathcal{G}}, \Omega, \delta^{\mathcal{G}})] |\psi(0)\rangle, \quad (\text{B9})$$

satisfies the transformation relation

$$|\psi_{\mathcal{G}^\Pi}(t)\rangle = \hat{U}_\Pi |\psi_{\mathcal{G}}(t)\rangle, \quad (\text{B10})$$

where we exploited the permutation invariance of the initial state  $|\psi(0)\rangle = |\mathbf{0}\rangle$ , i.e.  $\hat{U}_\Pi^\dagger |\mathbf{0}\rangle = |\mathbf{0}\rangle$ . Lastly, we insert the relation (B10) into the correlation matrix [Eq. (6)],

$$C_{i,j}^{\mathcal{G}}(t) = \langle \psi_{\mathcal{G}}(t) | \hat{n}_i \hat{n}_j | \psi_{\mathcal{G}}(t) \rangle, \quad (\text{B11})$$

leading to the final transformation relation (B4),

$$\begin{aligned} C_{i,j}^{\mathcal{G}^\Pi}(t) &= \langle \psi_{\mathcal{G}}(t) | \hat{n}_{\Pi^{-1}(i)} \hat{n}_{\Pi^{-1}(j)} | \psi_{\mathcal{G}}(t) \rangle \\ &= C_{\Pi^{-1}(i), \Pi^{-1}(j)}^{\mathcal{G}}(t). \end{aligned} \quad (\text{B12})$$

(3) To prove the last property we define a pair of isomorphic graphs  $\mathcal{G}_1$  and  $\mathcal{G}_2 = \mathcal{G}_1^\Pi$ . It remains to show the property

$$\kappa_{\text{GDQC}}(\mathcal{G}_1, \mathcal{G}_1^\Pi) = 1, \quad (\text{B13})$$

for the kernel function (B1). The property (B13) follows trivially from the GDQC feature vector invariance (B3), and the normalization of the feature vector  $\|\chi [C^{\mathcal{G}}(t), D^{\mathcal{G}}]\| = 1$ .  $\square$

### Appendix C: Expressiveness of GDQC

In this Appendix we prove the proposition 3: *The kernel function  $\kappa_{\text{GDQC}}$  (13) is as expressive as the GD-WL test given the latter is initialized with colors obtained from the multi-set of the values of the correlation matrix rows/columns.*

*Proof.* Consider the correlation matrix  $C_{i,j}^{\mathcal{G}}(t)$ , Eq. (B11). First, let's start by giving an example of how one can use the correlation matrix (at a fixed time step  $t$ ) as a color refinement algorithm. Let

$$q_t(i) = \text{hash} \left( \left\{ \left\{ C_{i,j}^{\mathcal{G}}(t) \ ; \ j \in \mathcal{V} \right\} \right\} \right), \quad (\text{C1})$$

be the color attributed to node  $i$  at time step  $t$  of the dynamics, where hash represents any injective function on its domain. Recall that GD-WL test can be formalized as :

$$\chi_{\mathcal{G}}^{(l)}(j) = \text{hash} \left( \left\{ \left\{ \left( D_{i,j}^{\mathcal{G}}, \chi_{\mathcal{G}}^{(l-1)}(i) \right) \ ; \ i \in \mathcal{V} \right\} \right\} \right). \quad (\text{C2})$$

In general, one starts with a uniform  $\chi_{\mathcal{G}}^{(0)}(j)$ , but in our case we put :

$$\chi_{\mathcal{G}}^{(0)}(j) = q_t(j). \quad (\text{C3})$$

Now, consider the following tensor

$$M_{i,j}^{\mathcal{G}} = \left( D_{i,j}^{\mathcal{G}}, \chi_{\mathcal{G}}^{(0)}(j) \right). \quad (\text{C4})$$

In order to prove the statement of proposition 4, we start by showing the following lemma :

**Lemma 5.** *Two graphs  $\mathcal{G}_1$  and  $\mathcal{G}_2$  are undistinguishable by the GD-WL test if and only if there is a permutation  $\Pi$  such that for every pair  $(i,j)$  we have:*

$$M_{i,j}^{\mathcal{G}_1} = M_{\Pi(i),\Pi(j)}^{\mathcal{G}_2}. \quad (\text{C5})$$

*Proof.* First we prove the *if* part. Suppose such a permutation exists, and call

$$R_{\mathcal{G}}^{(l)}(i) = \left\{ \left\{ \left( D_{i,j}^{\mathcal{G}}, \chi_{\mathcal{G}}^{(l)}(j) \right) \ : \ j \in \mathcal{V} \right\} \right\}, \quad (\text{C6})$$

the multi-set for node  $i$  corresponding to the data hashed in round  $l$ . Because we assume that this permutation exists, one must have :

$$\begin{aligned} R_{\mathcal{G}_1}^{(0)}(i) &= \left\{ \left\{ M_{i,j}^{\mathcal{G}_1} \ : \ j \in \mathcal{V}_1 \right\} \right\} = \left\{ \left\{ M_{\Pi(i),w}^{\mathcal{G}_2} \ : \ w \in \mathcal{V}_2 \right\} \right\} \\ &= R_{\mathcal{G}_2}^{(0)}(\Pi(i)), \end{aligned} \quad (\text{C7})$$

with  $w = \Pi(j)$ . This ensures that at the first round, vertex  $i$  in  $\mathcal{G}_1$  and vertex  $\Pi(i)$  in  $\mathcal{G}_2$  feed identical multi-sets into the hash function [cf. Eq. (C2)], and therefore receive the same color. Since by hypothesis we have  $D_{i,j}^{\mathcal{G}_1} = D_{\Pi(i),\Pi(j)}^{\mathcal{G}_2}$  for all  $(i,j)$ , we can also see that the multi-set hashed in the next round:

$$\begin{aligned} R_{\mathcal{G}_1}^{(1)}(i) &= \left\{ \left\{ \left( D_{i,j}^{\mathcal{G}_1}, \chi_{\mathcal{G}_1}^{(1)}(j) \right) \ : \ j \in \mathcal{V}_1 \right\} \right\} \\ &= \left\{ \left\{ \left( D_{\Pi(i),\Pi(j)}^{\mathcal{G}_2}, \chi_{\mathcal{G}_2}^{(1)}(\Pi(j)) \right) \ : \ j \in \mathcal{V}_1 \right\} \right\} \\ &= R_{\mathcal{G}_2}^{(1)}(\Pi(i)), \end{aligned} \quad (\text{C8})$$

leading to  $\chi_{\mathcal{G}_1}^{(2)}(i) = \chi_{\mathcal{G}_2}^{(2)}(\Pi(i))$ . The process repeats indefinitely until the number of iterations reaches its maximal value  $l_{\max}$ , and we thus have identical color classes on  $\mathcal{G}_1$  and  $\mathcal{G}_2$ , which means undistinguishability. Now we prove the *only if* part, i.e when the GD-WL process never separates the graphs, then such a permutation  $\Pi$  must exist. We know that after at most  $n$  iterations ( $n$  being the number of nodes in  $\mathcal{G}_1$  and  $\mathcal{G}_2$ ) the final colors, noted  $\chi^*$  appears the same number of times in each graph as they are assumed to be undistinguishable. If for each color class we choose a one-to-one correspondence between the vertices of  $\mathcal{G}_1$  and those of  $\mathcal{G}_2$  that share that color, we obtain a bijection

$$\Pi : \mathcal{V}_1 \mapsto \mathcal{V}_2, \quad \text{with} : \quad \chi_{\mathcal{G}_1}^*(i) = \chi_{\mathcal{G}_2}^*(\Pi(i)) \quad \forall i. \quad (\text{C9})$$

We now show by (downward) induction that

$$\chi_{\mathcal{G}_1}^{(l)}(i) = \chi_{\mathcal{G}_2}^{(l)}(\Pi(i)), \quad D_{i,j}^{\mathcal{G}_1} = D_{\Pi(i),\Pi(j)}^{\mathcal{G}_2}, \quad \forall (i,j), \quad (\text{C10})$$

where  $l \leq l_{\max}$ . The base case is  $l = l_{\max}$  which is exactly our Eq (C9). Now assume that (C10) holds, when colors at round  $l$  are computed, vertex  $i$  in  $\mathcal{G}_1$  hashes  $R_{\mathcal{G}_1}^{(l)}(i)$ . By the induction hypothesis we have  $R_{\mathcal{G}_1}^{(l-1)}(i) = R_{\mathcal{G}_2}^{(l-1)}(\Pi(i))$  which means that each ordered pair in  $R_{\mathcal{G}_1}^{(l-1)}(i)$  occurs with the same frequency in  $R_{\mathcal{G}_2}^{(l-1)}(\Pi(i))$ . This allows us to align each tuple with distance  $D_{i,j}^{\mathcal{G}_1}$  with the corresponding tuple  $D_{\Pi(i),\Pi(j)}^{\mathcal{G}_2}$ , as the distances don't change from one round to the other, ensuring that  $\chi_{\mathcal{G}_1}^{(l-1)}(j) = \chi_{\mathcal{G}_2}^{(l-1)}(\Pi(j))$  valid for  $\forall j \in \mathcal{V}_1$ .

One can then complete the downward induction to  $l = 0$  which shows

$$\begin{aligned} M_{i,j}^{\mathcal{G}_1} &= \left( D_{i,j}^{\mathcal{G}_1}, \chi_{\mathcal{G}_1}^{(0)}(j) \right) = \left( D_{\Pi(i),\Pi(j)}^{\mathcal{G}_2}, \chi_{\mathcal{G}_2}^{(0)}(\Pi(j)) \right) \\ &= M_{\Pi(i),\Pi(j)}^{\mathcal{G}_2}. \end{aligned} \quad (\text{C11})$$

Rewriting this for every  $(i,j)$  gives Eq. (C5).  $\square$

From here, the proof of proposition 3 is straightforward. If two graphs are undistinguishable by the GD-WL test with  $q_t(i)$  as initial coloring, then even when the number of bins is large enough (with maximal expressiveness attained when  $N_{\text{bins}}^D > \left[ \min \left( D_{i,j}^{\mathcal{G}} - D_{i',j'}^{\mathcal{G}} \right) \right]^{-1}$  and  $N_{\text{bins}}^C > \left[ \min \left( C_{i,j} - C_{i',j'} \right) \right]^{-1}$ ), according to lemma 5 their corresponding tensors  $M^{\mathcal{G}_1}$  and  $M^{\mathcal{G}_2}$  are one permutation away one from the other. Considering that hash is an injective function, this implies that, at a fixed graph distance value, the multi-sets obtained from the corresponding correlation matrix rows are also the same, and thus the number of times a given value for the correlation appears (while its corresponding nodes are at the same fixed distance) is also the same. Given the definition of the GDQC kernel, the corresponding feature vectors for such a pair of graphs are identical, and their kernel value is equal to 1, which completes the proof.  $\square$

## Appendix D: Kernel pooling statement

In this appendix, we demonstrate the claim of the proposition 4: For a set  $S = \{\kappa_1, \kappa_2, \dots, \kappa_N\}$  of graph kernels, let  $\kappa_A$  and  $\kappa_B$  be respectively the kernels obtained from pooling two subsets  $S_A$  and  $S_B$  of  $S$ . If  $S_A \subset S_B$  then  $\kappa_A$  is at least as expressive as  $\kappa_B$ .

We restrict this proof to the case of the two pooling operations described in this paper, the sum pooling (15) and the element-wise product pooling (16). It is enough to show that the expressiveness does not get lowered by adjoining new kernels to the set of pooled ones.

*Proof.* A (graph) kernel  $\kappa_B$  is more expressive than another (graph) kernel  $\kappa_A$  if there exists a given pair of non-isomorphic graphs  $\mathcal{G}_1$  &  $\mathcal{G}_2$  that  $\kappa_B$  can distinguish but not  $\kappa_A$ . Furthermore,  $\kappa_B$  must also be able to distinguish any such pair that  $\kappa_A$  distinguishes. For normalized kernels, this translates to  $\kappa_A(\mathcal{G}_1, \mathcal{G}_2) = 1$  and  $\kappa_B(\mathcal{G}_1, \mathcal{G}_2) < 1$ . Hereby, we adopt the convention that isomorphic graphs should have a maximal kernel value, which is 1 when the kernel is normalized. over

First we need to fix the weight updating rule that ensures comparability between the kernels  $\kappa_A$  and  $\kappa_B$  in the case of sum pooling,

$$\kappa_{A,+}(\mathcal{G}_1, \mathcal{G}_2) = \sum_{i=1}^{n_A} \alpha_i \kappa_i(\mathcal{G}_1, \mathcal{G}_2), \quad (\text{D1})$$

where  $S_A = \{\kappa_1, \dots, \kappa_{n_A}\}$  and  $\sum_{i=1}^{n_A} \alpha_i = 1$  which then

becomes (after enriching the pooling set) :

$$\kappa_{B,+}(\mathcal{G}_1, \mathcal{G}_2) = \sum_{i=1}^{n_A} \alpha'_i \kappa_i(\mathcal{G}_1, \mathcal{G}_2) + \sum_{i=n_A+1}^{n_B} \alpha'_i \kappa_i(\mathcal{G}_1, \mathcal{G}_2), \quad (\text{D2})$$

where  $S_B = \{S_A, \kappa_{n_A+1}, \dots, \kappa_{n_B}\}$  and  $\sum_{i=1}^{n_B} \alpha'_i = 1$ . To ensure the evaluation of the set adjoining operation, we have to consider the case where the update of the weights only introduces a factor that is proportional to the relative set sizes *i.e.* :

$$\left(\sum_{i=1}^{n_A} \alpha'_i\right) / \left(\sum_{i=1}^{n_B} \alpha'_i\right) = |S_A| / |S_B|, \quad (\text{D3})$$

which is obtained when  $\alpha'_i = \alpha_i n_A / n_B$ . Next we can list the two following cases :

$$\kappa_{+,B}(\mathcal{G}_1, \mathcal{G}_2) = \frac{n_A}{n_B} \kappa_{+,A}(\mathcal{G}_1, \mathcal{G}_2) + \sum_{i=n_A+1}^{n_B} \alpha'_i \kappa_i(\mathcal{G}_1, \mathcal{G}_2), \quad (\text{D4})$$

and

$$\kappa_{\times,B}(\mathcal{G}_1, \mathcal{G}_2) = \kappa_{\times,A}(\mathcal{G}_1, \mathcal{G}_2) \prod_{i=n_A+1}^{n_B} \kappa_i(\mathcal{G}_1, \mathcal{G}_2). \quad (\text{D5})$$

So if  $\kappa_{\times,A} = 1$  then  $\kappa_{\times,B} \leq 1$  provided that  $\kappa_i(\mathcal{G}_1, \mathcal{G}_2)$ .

Now if there is at least one kernel  $\kappa_i \in \{\kappa_{n_A+1}, \dots, \kappa_{n_B}\}$  such that  $\kappa_i(\mathcal{G}_1, \mathcal{G}_2) < 1$  then it directly follows from the two previous equations that  $\kappa_{+,B} < \kappa_{+,A}$  and  $\kappa_{\times,B} < \kappa_{\times,A}$ . This assumption is not necessarily true, and in the case where  $\kappa_i(\mathcal{G}_1, \mathcal{G}_2) = 1 \quad \forall \quad \kappa_i \in \{\kappa_{n_A+1}, \dots, \kappa_{n_B}\}$  then we have  $\kappa_{+,B} = \kappa_{+,A}$  and  $\kappa_{\times,B} = \kappa_{\times,A}$ . This allows us to state that without any specific knowledge of  $\{\kappa_{n_A+1}, \dots, \kappa_{n_B}\}$  that  $\kappa_{+,B} \leq \kappa_{+,A}$  and  $\kappa_{\times,B} \leq \kappa_{\times,A}$ .  $\square$

- 
- [1] K. Sharma, Y.-C. Lee, S. Nambi, A. Salian, S. Shah, S.-W. Kim, and S. Kumar, A survey of graph neural networks for social recommender systems, *ACM Comput. Surv.* **56**, 10.1145/3661821 (2024).
  - [2] J. Gilmer, S. S. Schoenholz, P. F. Riley, O. Vinyals, and G. E. Dahl, *Neural message passing for quantum chemistry* (2017), arXiv:1704.01212 [cs.LG].
  - [3] M. Allamanis, M. Brockschmidt, and M. Khademi, Learning to represent programs with graphs, in *International Conference on Learning Representations* (2018).
  - [4] M. Xu and L. Chang, Graph edit distance estimation: A new heuristic and a holistic evaluation of learning-based methods, *Proc. ACM Manag. Data* **3**, 10.1145/3725304 (2025).
  - [5] S. Vishwanathan, N. N. Schraudolph, R. Kondor, and K. M. Borgwardt, Graph kernels, *Journal of Machine Learning Research* **11**, 1201 (2010).
  - [6] N. Shervashidze, P. Schweitzer, E. J. van Leeuwen, K. Mehlhorn, and K. M. Borgwardt, Weisfeiler-Lehman graph kernels, *Journal of Machine Learning Research* **12**, 2539 (2011).
  - [7] G. Peyré, M. Cuturi, and J. Solomon, Gromov-Wasserstein averaging of kernel and distance matrices, in *Proc. 33rd International Conference on Machine Learning*, Proc. 33rd International Conference on Machine Learning (New-York, United States, 2016).
  - [8] M. M. Bronstein, J. Bruna, Y. LeCun, A. Szlam, and P. Vandergheynst, Geometric deep learning: Going beyond Euclidean data, *IEEE Signal Processing Magazine* **34**, 18 (2017).
  - [9] L. Rossi, A. Torsello, and E. R. Hancock, A continuous-time quantum walk kernel for unattributed graphs, in *Graph-Based Representations in Pattern Recognition*, edited by W. G. Kropatsch, N. M. Artner, Y. Haxhimusa, and X. Jiang (Springer Berlin Heidelberg, Berlin, Heidelberg, 2013) pp. 101–110.
  - [10] S. Thabet, M. Djellabi, I. O. Sokolov, S. Kasture, L.-P. Henry, and L. Henriet, Quantum positional encodings for graph neural networks, in *Proceedings of the 41st International Conference on Machine Learning*, ICML'24 (JMLR.org, 2024).

- [11] L. Bai, L. Rossi, A. Torsello, and E. R. Hancock, A quantum Jensen–Shannon graph kernel for unattributed graphs, *Pattern Recognition* **48**, 344 (2015).
- [12] V. Sabarad, V. Varma, and T. S. Mahesh, *Experimental machine learning with classical and quantum data via NMR quantum kernels* (2025), [arXiv:2412.09557 \[quant-ph\]](https://arxiv.org/abs/2412.09557).
- [13] L.-P. Henry, S. Thabet, C. Dalyac, and L. Henriët, Quantum evolution kernel: Machine learning on graphs with programmable arrays of qubits, *Phys. Rev. A* **104**, 032416 (2021).
- [14] B. Albrecht, C. Dalyac, L. Leclerc, L. Ortiz-Gutiérrez, S. Thabet, M. D’Arcangelo, J. R. K. Cline, V. E. Elfving, L. Lassablière, H. Silvério, B. Ximenez, L.-P. Henry, A. Signoles, and L. Henriët, Quantum feature maps for graph machine learning on a neutral atom quantum processor, *Phys. Rev. A* **107**, 042615 (2023).
- [15] pasqal-io, quantum-evolution-kernel: A graph machine learning library using quantum computing, <https://github.com/pasqal-io/quantum-evolution-kernel> (2025), accessed: 2025-07-18; Latest release: v0.3.3 (June 6, 2025).
- [16] L. Bai, L. Rossi, H. Bunke, and E. R. Hancock, Attributed graph kernels using the Jensen–Tsallis  $q$ -differences, in *Machine Learning and Knowledge Discovery in Databases*, edited by T. Calders, F. Esposito, E. Hüllermeier, and R. Meo (Springer Berlin Heidelberg, Berlin, Heidelberg, 2014) pp. 99–114.
- [17] T. F. Gallagher, *Rydberg Atoms*, Cambridge Monographs on Atomic, Molecular and Chemical Physics (Cambridge University Press, 1994).
- [18] A. K. Debnath, R. L. Lopez de Compadre, G. Debnath, A. J. Shusterman, and C. Hansch, Structure-activity relationship of mutagenic aromatic and heteroaromatic nitro compounds. correlation with molecular orbital energies and hydrophobicity, *Journal of Medicinal Chemistry* **34**, 786 (1991).
- [19] C. Helma and S. Kramer, A survey of the predictive toxicology challenge 2000–2001, *Bioinformatics* **19**, 1179 (2003).
- [20] C. Morris, N. M. Kriege, F. Bause, K. Kersting, P. Mutzel, and M. Neumann, TUDataset: A collection of benchmark datasets for learning with graphs, *CoRR* **abs/2007.08663** (2020), 2007.08663.
- [21] A. Browaeys and T. Lahaye, Many-body physics with individually controlled Rydberg atoms, *Nature Physics* **16**, 132 (2020).
- [22] G. A., M. Y., W. T., C. A., V. M., C. D., P. P., B. A., and G. Ph., Observation of collective excitation of two individual atoms in the Rydberg blockade regime, *Nature Physics* **5**, 115 (2009).
- [23] B. N. Clark, C. J. Colbourn, and D. S. Johnson, Unit disk graphs, *Discrete Mathematics* **86**, 165 (1990).
- [24] F. Kuhn, T. Moscibroda, and R. Wattenhofer, Unit disk graph approximation, in *Proceedings of the 2004 Joint Workshop on Foundations of Mobile Computing*, DIALM-POMC ’04 (Association for Computing Machinery, New York, NY, USA, 2004) pp. 17–23.
- [25] PubChem, National Center for Biotechnology Information (NCBI), U.S. National Library of Medicine, Periodic table of elements, <https://pubchem.ncbi.nlm.nih.gov/periodic-table/>, accessed: 2025-08-29.
- [26] H. Silvério, S. Grijalva, C. Dalyac, L. Leclerc, P. J. Karalekas, N. Shammah, M. Beji, L.-P. Henry, and L. Henriët, Pulser: An open-source package for the design of pulse sequences in programmable neutral-atom arrays, *Quantum* **6**, 629 (2022).
- [27] K. Bidzhiev, S. Grava, P. le Henaff, M. Mendizabel Pico, E. Merhej, and A. Quelle, *pasqal emulators* (2025).
- [28] N. Aronszajn, Theory of reproducing kernels, *Transactions of the American Mathematical Society* **68**, 337 (1950).
- [29] B. Schölkopf, R. Herbrich, and A. J. Smola, A generalized representer theorem, in *Proceedings of the 14th Annual Conference on Computational Learning Theory and 5th European Conference on Computational Learning Theory*, COLT ’01/EuroCOLT ’01 (Springer-Verlag, Berlin, Heidelberg, 2001) pp. 416–426.
- [30] J. Mercer, Functions of positive and negative type, and their connection with the theory of integral equations, *Philosophical Transactions of the Royal Society of London* **209**, 415 (1909).
- [31] B. Schölkopf and A. J. Smola, *Learning with kernels: support vector machines, regularization, optimization, and beyond*, Adaptive computation and machine learning (MIT Press, 2002).
- [32] C. Cortes and V. Vapnik, Support-vector networks, *Machine Learning* **20**, 273 (1995).
- [33] T. Gärtner, P. Flach, and S. Wrobel, On graph kernels: Hardness results and efficient alternatives, in *Learning Theory and Kernel Machines*, edited by B. Schölkopf and M. K. Warmuth (Springer Berlin Heidelberg, Berlin, Heidelberg, 2003) pp. 129–143.
- [34] G. Nikolettos, P. Meladianos, S. Limnios, and M. Vazirgiannis, A degeneracy framework for graph similarity, in *Proceedings of the Twenty-Seventh International Joint Conference on Artificial Intelligence, IJCAI-18* (International Joint Conferences on Artificial Intelligence Organization, 2018) pp. 2595–2601.
- [35] K. M. Borgwardt and H.-P. Kriegel, Shortest-path kernels on graphs, in *Proceedings of the Fifth IEEE International Conference on Data Mining*, ICDM ’05 (IEEE Computer Society, USA, 2005) pp. 74–81.
- [36] Y. Gurevich, From invariants to canonization, in *Bulletin of the European Association for Theoretical Computer Science*, Vol. 63 (1997).
- [37] B. Zhang, S. Luo, L. Wang, and D. He, Rethinking the expressive power of GNNs via graph biconnectivity, in *The Eleventh International Conference on Learning Representations* (2023).
- [38] B. Zhang, L. Zhao, and H. Maron, On the expressive power of spectral invariant graph neural networks, in *Proceedings of the 41st International Conference on Machine Learning*, ICML’24 (JMLR.org, 2024).
- [39] C. Godsil and G. F. Royle, *Algebraic Graph Theory*, Graduate Texts in Mathematics No. Book 207 (Springer, 2001).
- [40] C. Bodnar, F. Frasca, Y. Wang, N. Otter, G. F. Montufar, P. Lió, and M. Bronstein, Weisfeiler and Lehman go topological: Message passing simplicial networks, in *Proceedings of the 38th International Conference on Machine Learning*, Proceedings of Machine Learning Research, Vol. 139, edited by M. Meila and T. Zhang (PMLR, 2021) pp. 1026–1037.
- [41] N. Pržulj, Biological network comparison using graphlet degree distribution, *Bioinformatics* **23**, e177 (2007).
- [42] S. B. Seidman, Network structure and minimum degree, *Social Networks* **5**, 269 (1983).
- [43] N. M. Kriege, P.-L. Giscard, and R. Wilson, On valid optimal assignment kernels and applications to graph classification, in *Advances in Neural Information Processing Systems*, Vol. 29, edited by D. Lee, M. Sugiyama, U. Luxburg, I. Guyon, and R. Garnett (Curran Associates, Inc., 2016).
- [44] G. Siglidis, G. Nikolettos, S. Limnios, C. Giatsidis, K. Skianis, and M. Vazirgiannis, Grakel: A graph kernel library in python, *Journal of Machine Learning Research* **21**, 1 (2020).
- [45] M. Reed and B. Simon, *Methods of Modern Mathematical Physics, Vol. IV: Analysis of Operators* (Academic Press, New York, 1978).
- [46] T. Kato, *Perturbation Theory for Linear Operators*, 2nd ed., Classics in Mathematics (Springer, Berlin, Heidelberg, 1995).